



Investigation on the tribocorrosion and electrochemical corrosion behaviour of AA2014/Al₂O₃ nanocomposites fabricated through ultrasonication coupled stir-squeeze casting method

A. Gnanavelbabu¹ · X. Jerish Amul¹ · K. T. Sunu Surendran¹

Received: 22 July 2021 / Accepted: 1 January 2022 / Published online: 24 January 2022
© The Author(s), under exclusive licence to Springer Nature B.V. 2022

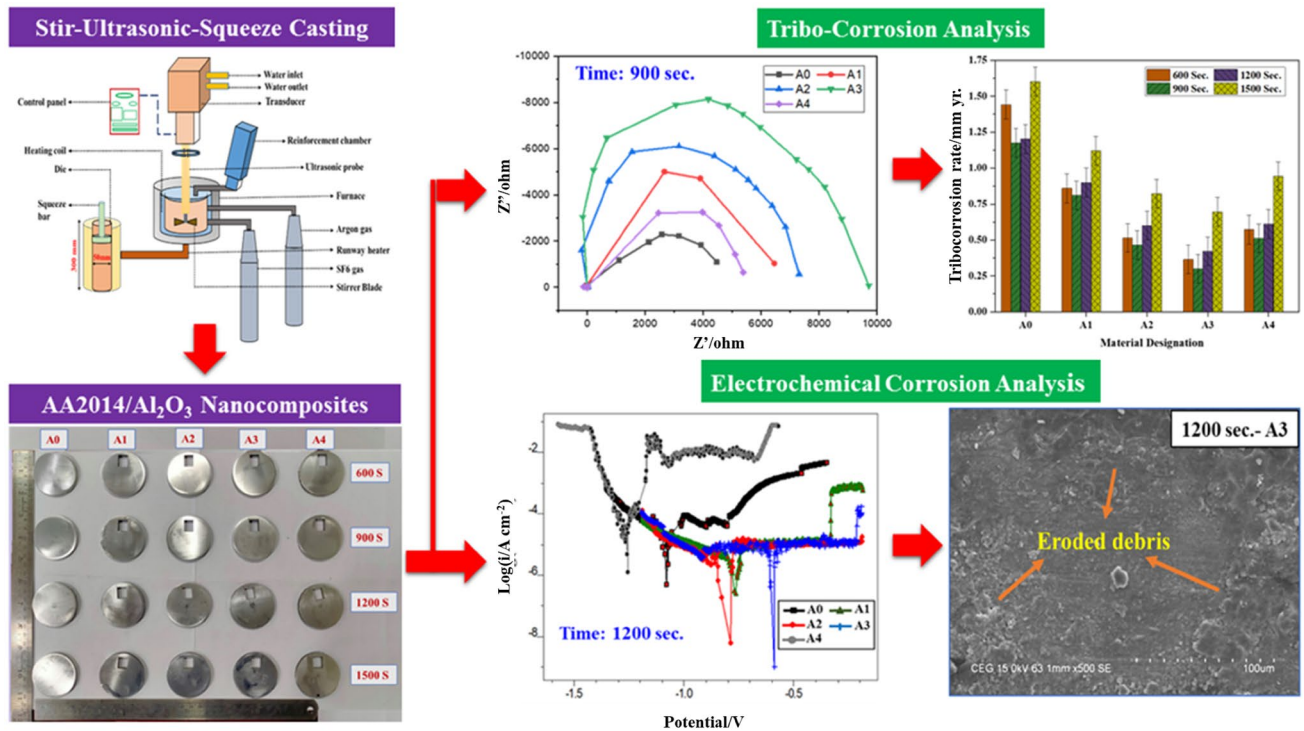
Abstract

In this work, the tribocorrosion and electrochemical corrosion behaviour of AA2014/Al₂O₃ (1–4 wt%) nanocomposites were investigated. An unreinforced 2014 alloy and the proposed nanocomposites were prepared through ultrasonication coupled stir-squeeze casting method followed by solutionizing at 510 °C for 2 h and ageing at 165 °C for 16 h. Studies on the dispersion of nanoparticles, intermetallic phase formation, porosity, and hardness were carried out prior to the corrosion analysis. Tribocorrosion test was performed in a linear reciprocating tribometer using 3.5 wt% NaCl solution as electrolyte under potentiodynamic polarization condition for an exposure period of 600, 900, 1200, and 1500 s. A similar testing condition was applied while performing the electrochemical test of materials in a cylindrical beaker. The experimental results indicated a uniform distribution of nanoparticles and the formation of β-CuAl₂ phase in the nanocomposites. A maximum hardness of 150 HV was obtained for the nanocomposite reinforced with 2 wt% of Al₂O₃. Tribocorrosion test results indicated that AA2014/3 wt% Al₂O₃ nanocomposite exhibit the lowest potential of –0.62 to –0.68 V with a friction coefficient of 0.15 μ and a minimum current density of 4.889×10^{-4} at 900 s. The same nanocomposite reduced the removal of metal ions with the lowest potential range of –0.4 to –0.5 V and decreased current density of 1.521×10^{-5} at 1200 s. during the electrochemical test. Alumina hydroxide films and secondary phases caused a superior corrosion resistance at higher exposure times. The microstructural analysis of the corroded surfaces showed pitting corrosion, formation of pits and cracks.

✉ A. Gnanavelbabu
agbabu@annauniv.edu

¹ Department of Industrial Engineering, CEG Campus, Anna University, Chennai 600025, India

Graphical abstract



Keywords Aluminium nanocomposites · Ultrasonication · Tribocorrosion · Electrochemical corrosion

1 Introduction

Marine environments certainly accelerate the degradation of offshore equipment through corrosion and consequently decrease their operating life span [1]. Aluminium alloys are lightweight-corrosion resistant materials used in marine and aerospace applications to reduce the overall weight and increase working performance [2, 3]. Aluminium alloy 2014 is typically used in aerospace applications such as water ballast tanks [4]. Even though AA2014 has better corrosion resistivity, they are susceptible to chloride solution forming oxidation and pitting. Therefore, to increase corrosion resistance, AA2014 is reinforced with non-metallic ceramic particles such as Al₂O₃, SiC, B₄C, TiB₂, ZrB₂, etc., [5]. Among these, alumina nanoparticles improve aluminium alloys mechanical and anti-corrosion properties [6, 7]. Furthermore, alumina nanoparticulate reinforcements with a high surface area to volume ratio significantly impact composite properties [8].

The stir coupled squeeze cast process is one of the most widely used casting processes for producing aluminium metal matrix composites [9–11]. Because of the immense squeeze pressure, the molten metal in the mold acquires both casting and forging properties [12, 13]. This improves

physical and mechanical properties while also refining the microstructure [14, 15]. The conventional stir casting method necessitates a longer stirring period, which oxidizes the matrix and obstructs reinforcement dispersion in the matrix due to agglomeration and low wettability [16]. To tackle these issues, a novel Ultrasonication Treatment (UST) is used to improve nanoparticle dispersion by imploding particle clusters, the wettability, and facilitating degassing [17–20]. Deng et al. [21] stated that nano-sized particle dispersion in the matrix generates clusters and agglomeration due to the high surface-to-volume ratio. Gnanavelbabu et al. [22] used ultrasonication to achieve a fine dispersion of nanoparticles in the matrix and to minimize porosity. T6 heat treatment is recommended for achieving a refined grain structure. Sharma et al. [23] discovered that composites heat-treated at T6 improved their properties more than composites heat-treated at T4.

Nowadays, researchers are paying more attention to studies on the electrochemical and tribocorrosion corrosion behaviour of alloys and composites. Tribocorrosion experiments, in general, examine the wear-induced corrosive behaviour of materials subjected to particular corrosive media under defined testing conditions. Murthy et al. [24] found that aluminium is extremely corrosive in marine sectors due to the presence

of impurities with high electronegative potential such as Fe, Cu, and Ni. Fang et al. [25] improved an aluminium alloys mechanical and corrosion properties using numerous oxide-based reinforcements such as Y_2O_3 , Al_2O_3 , and ZrO_2 . According to Sundar and Qi [26], the addition of Al_2O_3 results in higher stiffness, finer microstructure, and superior polarization behaviour, resulting in higher corrosion resistance. Jun et al. [27] reported that the combination of wear and corrosion accelerates material degradation due to improved corrosion potential. Cheng et al. [28] demonstrated that increasing the alumina content reduces the coefficient of friction during the tribocorrosion test. In comparison, adding a large amount of Al_2O_3 resulted in a higher corrosion resistivity in 3.5 wt% NaCl solution. Huttunen et al. [29] concluded that wear-induced corrosion accounted for nearly 99% of material losses at anodic potentials when the load was 10 N, but just about 20% when the load was 20 N. Olatunji and Esther [30] investigated the relationship between wear and corrosion in aluminium alloys using open-circuit potential, polarization, and electrochemical impedance.

According to Sinhmar and Dwivedi [31], the Al_2Cu phase accelerates anodic and cathodic reactivity in AA2014 alloy, modifying the microstructure and increasing electrochemical resistivity between weld joints. Gharavi et al. [32] performed an electrochemical test on an aluminium alloy and found pitting and inter-granular corrosion in weld areas because electrolyte causes corrosion at grain boundaries. According to Roseline and Paramasivam [33], heat-treated zirconia alumina reinforced aluminium alloy eliminates corrosion and increases current density while decreasing volume percentage. Hurtado and Sundaram [34] discovered that intermetallic phases play a significant role in corrosion potential, and the tafel polarization findings show that increasing alumina oxide has little impact on corrosion resistance.

According to reviews of the literature, the inclusion of alumina oxide nanoparticles would improve the mechanical and corrosive properties of aluminium alloy. A review of the existing literatures further reveals a need for investigation into the corrosion behaviour of aluminium/ Al_2O_3 nanocomposites. Despite this, only a few studies on the tribocorrosion and electrochemical corrosion behaviour of aluminium nanocomposites have been published. Therefore, the corrosion behaviour of AA2014/ Al_2O_3 (1–4 wt%) nanocomposites fabricated using the ultrasonication coupled stir-squeeze casting followed by the T6 heat treatment process was investigated in this work. The corrosion behaviour of proposed nanocomposites in 3.5 wt% NaCl solution was investigated using tribo-corrosion and electrochemical test methods, at exposure times of 600, 900,

1200, and 1500 s. The corrosion rate and corrosion mechanism are explained through charge transfer, diffusion and absorption of ions using electrochemical impedance spectroscopy. SEM and optical images are used for analysing the corroded surface.

2 Materials and experimental procedure

2.1 Matrix and reinforcement materials

The AA2014 was used as matrix material in this work. Table 1 shows the result of elemental analysis of AA2014. The reinforcing material was Alumina nanopowder with an average particle size of 20–30 nm. Table 2 shows the fundamental properties of AA2014 and Al_2O_3 .

2.2 Fabrication of AA2014/ Al_2O_3 nanocomposites

An illustration of ultrasonication coupled stir-squeeze casting equipment (supplied by SwamEquip, India) employed in this work is shown in Fig. 1. As demonstrated in the figure, the fabrication process was carried out in an Argon gas-protected environment for better quality casting. Initially, 2014 alloy billets were heated in an electrical resistance furnace up to a liquidous temperature of 700 °C. The mechanical stirrer was then inserted into the molten metal for performing vigorous stirring at a speed of 500 rpm for 10 min. During the stirring, the preheated (300 °C for 1 h) alumina nanopowder was added to the melt using a powder feeder set up attached with the equipment. After sufficient stirring, the ultrasonic probe was inserted in the melt for performing ultrasonication at 20 kHz/2.5 kW for 5 min. During ultrasonication, water was circulated around the transducer to minimize heat generation. After the sufficient mixing of nanoparticles in the matrix through stirring and ultrasonication, the bottom-pouring valve was opened. The melt was transferred into a steel die preheated at 300 °C

Table 2 Fundamental properties of AA2014 and Al_2O_3 [36–38]

Properties	AA2014	Al_2O_3
Density ($g\ cm^{-3}$)	2.81	3.91
Melting temperature (°C)	510	2055
Coefficient of thermal expansion (K^{-1})	23.4×10^{-6}	7.5×10^{-6}

Table 1 Constituent elements of AA2014 [35]

Element	Mn	Mg	Fe	Cr	Zn	Cu	Si	Ti	Al
wt%	0.4	0.8	0.7	0.1	0.15	3.9	0.70	0.2	Balance

Fig. 1 Illustration of ultra-sonication coupled stir-squeeze casting setup

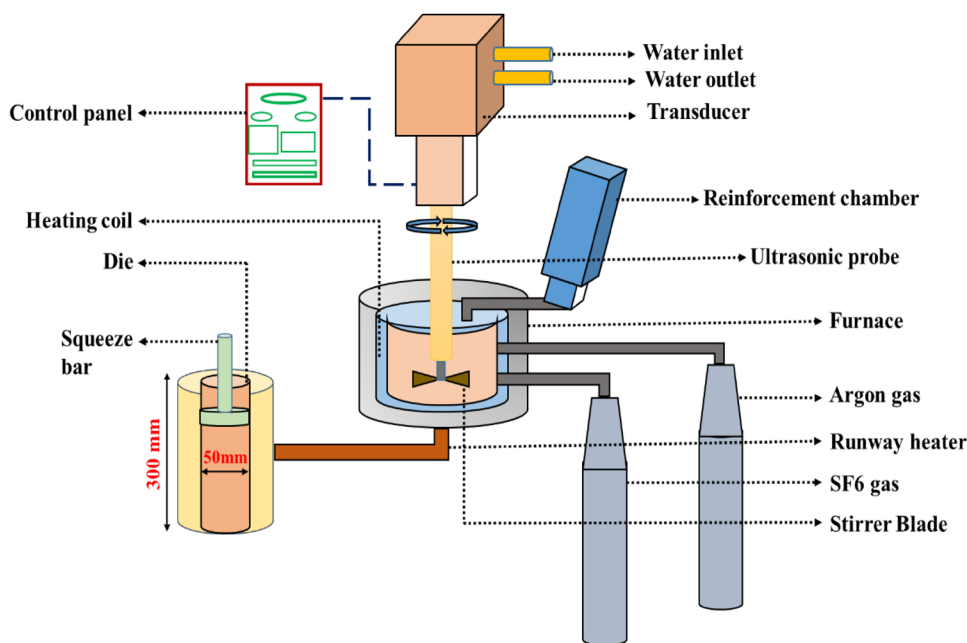


Table 3 Composition and designation of materials

S. No	Composition	Designation
1	AA2014	A0
2	AA2014+1 wt% Al ₂ O ₃	A1
3	AA2014+2 wt% Al ₂ O ₃	A2
4	AA2014+3 wt% Al ₂ O ₃	A3
5	AA2014+4 wt% Al ₂ O ₃	A4

for 1 h. The dimension of the cylindrical die was $\phi 50$ mm and depth 300 mm. immediately after the filling of melt, squeezing was done on the melt for 1 min at a squeeze pressure of 150 MPa. Specimens were taken from the die after solidification. Following this procedure, four nanocomposites AA2014/Al₂O₃ (1–4 wt%) and an unreinforced alloy were fabricated. Table 3 shows the composition of materials and their designations.

2.3 Heat treatment

The fabricated alloy and nanocomposites were then heat-treated at T6 condition using a muffle furnace (Servo Enterprises, India). Heat treatment was carried out under an argon gas-protected environment at a heating rate of 3 °C/min. Initially, solutionizing (T4) at 510 °C for 2 h was carried out. Materials were then rapidly quenched in water kept at 25 °C. Finally, ageing at 165 °C for 14 h followed by air-cooling was performed. The heat treatment furnace setup and graphical representation of the heat treatment cycle (T6) are shown in Figs. 2 and 3 respectively.

2.4 Density and porosity measurement

The porosity of the materials was calculated using the Archimedes principle (experimental density) and the rule of mixtures (theoretical density). Theoretical and experimental density was calculated using Eqs. (1 and 2), respectively. The sample was weighed in the air and in water to determine the experimental density. All samples were weighed at least three times using a digital weighing balance machine with an accuracy of ± 0.001 g and the average value was taken.

$$\rho_{\text{act}} = \frac{W_{\text{air}}}{W_{\text{air}} - W_{\text{water}}} \times \rho_{\text{water}} \quad (1)$$

$$P = 1 - \frac{\rho_{\text{act}}}{\rho_{\text{theo}}} \times 100 \quad (2)$$

where ρ_{act} —Actual density of material in the air (g cc^{-1}), ρ_{water} —Actual density of material in water (g cc^{-1}), W_{air} —Weight of the material in the air (g), W_{water} —Weight of the material in water (g), P —Porosity (%), ρ_{act} —Actual density (g cc^{-1}), ρ_{theo} —Theoretical density (g cc^{-1}).

2.5 Microstructure and interphase analysis

The microstructural characterization of alloy and nanocomposites was done using High-Resolution Scanning Electron Microscope (HR-SEM) (FEI-Quanta FEG 200F) images. Samples were polished with SiC abrasive papers of 220–2000 grades on a double-disc polisher machine to achieve a clear microstructural image. Diamond paste (1 μm)

Fig. 2 a Muffle furnace with a controlled environment, b PID controller, and c Heating chamber setup

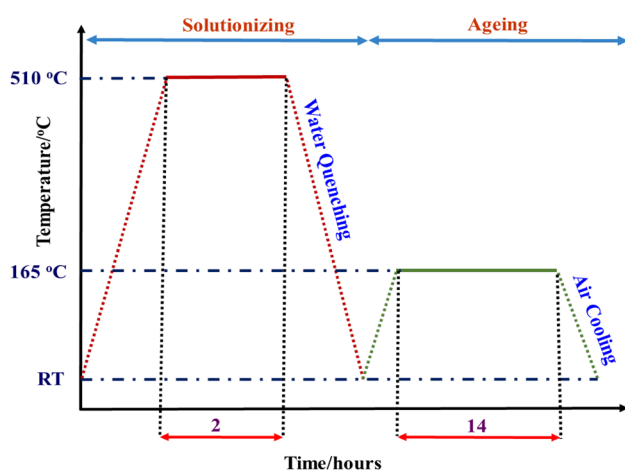
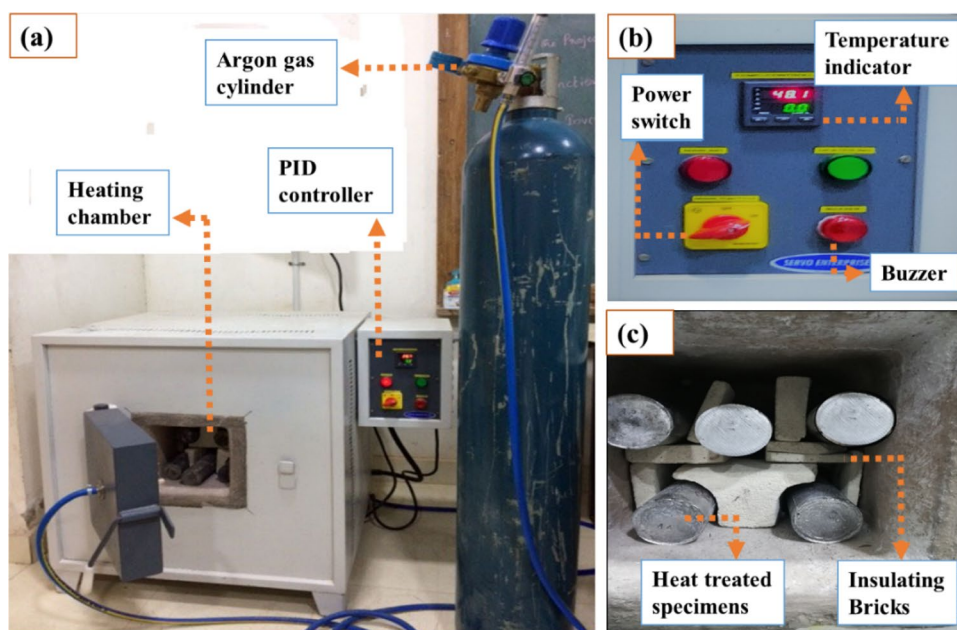


Fig. 3 Graphical representation of T6 heat treatment process

mixed with distilled water was used for getting an ultra-fine surface finish. Keller reagent (10 ml HF acid, 15 ml HCl acid, 25 ml HNO₃ acid, and 50 ml distilled water) was used to etch the samples for 5 s to expose their grain boundaries and orientations. The intermetallic phase analysis of alloy and composites was carried out using the XRD diffractometer (Bruker D8 Discover). The samples were scanned at step rate at an angle of 0.15° at 40 kV, 40 mA, 2.2 kW using Cu α radiation ($\alpha = 1.54186 \text{ \AA}$).

2.6 Hardness test

The hardness test was carried out as per ASTM standard E384-17 on a Vickers microhardness tester (Leitz

Wetzlar). At 500 g load, a diamond probe with an angle of 136° was indented for 15 s. The specimen's hardness was measured using an average of five measurements.

2.7 Tribocorrosion test

Tribocorrosion test was carried out in a linear reciprocating tribometer (Ducom, India) equipped with a corrosion test module. The tribometer was coupled with an anti-corrosive cup for filling electrolyte solution, as shown in Fig. 4. The reference electrode was a saturated calomel electrode (SCE), and the counter electrode was graphite. Samples having an exposure area of 20 mm² were the working electrode. The moving body was a hardened pin (steel) against a static counter material (specimen of $\phi 50$ mm and thickness 5 mm). A stroke length of 10 mm, frequency of 4 Hz, a normal load of 20 N was applied for various exposure times of 600, 900, 1200, and 1500 s. The open-circuit polarization was measured during, prior, and after sliding. At a ± 0.5 V electric potential and a scanning rate of 2 mV s⁻¹, the tafel was explored. Using the tafel curve, corrosion rate, I_{corr} (corrosion current), and E_{corr} (corrosion potential) were determined. Thus, the tafel exploration technique was used to determine the corrosion rate of specimens. The surface morphology of tested specimens was analyzed using SEM images. Before the test, the samples were polished with SiC fine paper and cleaned with acetone. The samples before conducting the tribocorrosion tests are shown in Fig. 5.

Fig. 4 Schematic representation of tribocorrosion test setup

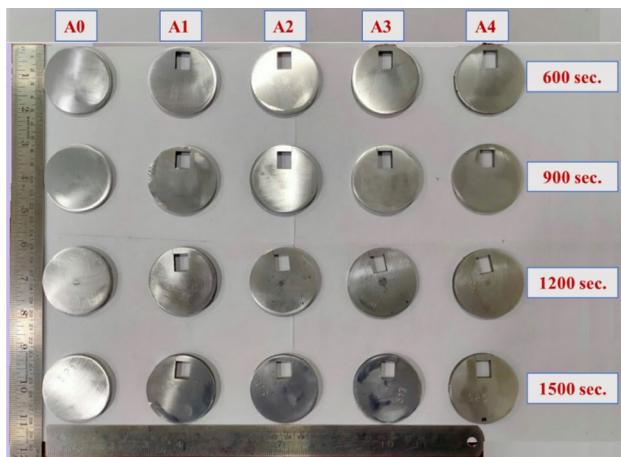
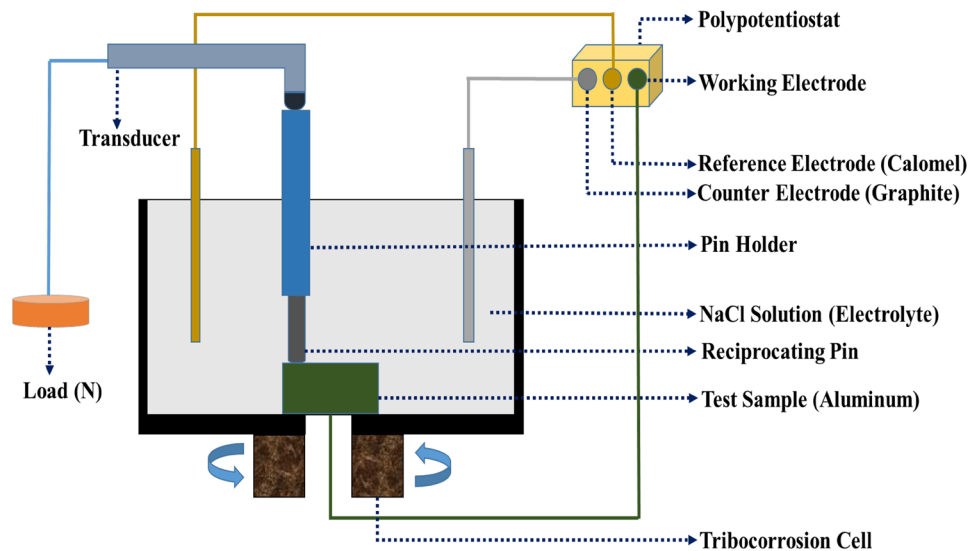


Fig. 5 Polished alloy and nanocomposite specimens for tribocorrosion test

2.8 Electrochemical corrosion test

A schematic illustration of the electrochemical test is provided in Fig. 6. As shown in the figure, in the setup, the working electrode was the testing sample, while the counter and reference electrodes were a platinum cell and a SCE, respectively. A specimen with a diameter of 50 mm and a thickness of 5 mm was used for electrochemical testing. At room temperature, the samples were placed in an anti-corrosive glass beaker filled with a 3.5 wt% NaCl solution. According to ASTM standard G31-72, the pH value was maintained between 6.5 and 7. The samples were exposed for 600, 900, 1200, and 1500 s. Polarization curves from -0.5 to $+0.5$ mV were obtained at a constant 2 mV s^{-1} sweep rate. Both anodic and cathodic polarization curves were recorded using a corrosion measurement system Ivium Soft (10 kHz to 0.1 Hz). Corrosion current density value was

calculated using the tafel extrapolation method at an interval of 10 nA to 1 A. After each experiment, the electrolyte was changed. To remove the corroded products formed on the surface, the water rinsed samples were cleaned with acetone. The corrosion products were removed for both testing using chromic acid ($180 \text{ g l}^{-1} \text{ CrO}_3$) and silver nitrate solution ($10 \text{ g l}^{-1} \text{ AgNO}_3$) according to ASTM G1-03.

3 Results and discussion

3.1 Density and porosity

Table 4 shows the density and porosity of the fabricated materials. The actual density of the fabricated materials is significantly lower than the theoretical density. The porosity of nanocomposites increased as the amount of nanoparticles increased. Because the nanoparticles have a high surface-to-volume ratio, they tend to stick together. This causes the formation of clusters of nanoparticles. Therefore, a significant volume of nano-sized reinforcing particles-induced agglomeration in the matrix, lowering the actual density and increasing porosity [39]. However, the porosity of nanocomposites was improved due to the homogenous dispersion of reinforced particles in the matrix through mechanical stirring and ultrasonication. Furthermore, the squeeze pressure facilitates shrinkage porosity reduction and microstructure refinement [40].

3.2 Particle dispersion and intermetallic phase analysis

Figure 7a shows the SEM image AA2014 alloy. The figure indicates the primary (α -Al) and secondary phases (β -CuAl₂) of alloy. HR-SEM images were used to analyze

Fig. 6 Schematic illustration of the electrochemical corrosion test arrangement

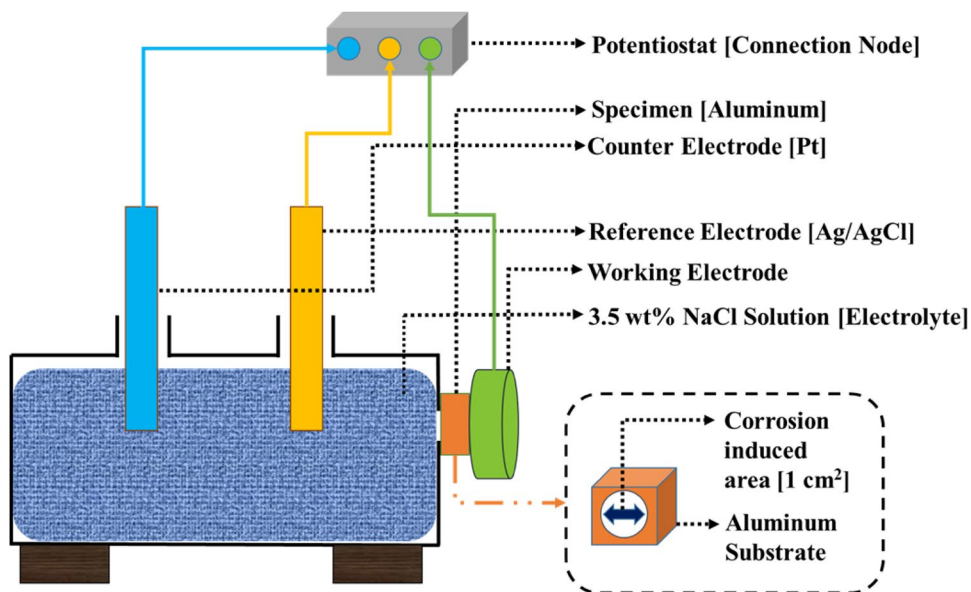


Table 4 Density and porosity of fabricated materials

S.no	Material designation	The. density (g cm ⁻³)	Act. density (g cm ⁻³)	Porosity (%)
1	A0	2.8101	2.7990	0.395
2	A1	2.8213	2.8095	0.418
3	A2	2.8232	2.8113	0.421
4	A3	2.8274	2.8145	0.456
5	A4	2.8290	2.8155	0.477

the dispersion of Al₂O₃ nanoparticles in the AA2014 matrix. Figure 7b–e shows the distribution of nanoparticles in the matrix. The stirring and UST uniformly dispersed the alumina particles in the matrix at 1 and 2 wt% of alumina, while adding an excess amount of reinforcements formed tiny clusters of nanoparticles as seen in Fig. 7d and e. The XRD test results of the materials are illustrated in Fig. 8. The diffraction pattern of alloy indicates the peaks of α -Al phase and β -CuAl₂ intermetallic phase, as shown in Fig. 8a. The XRD pattern of AA2014/Al₂O₃ nanocomposite is given in Fig. 8b. In the figure, in addition to the α -Al and β -CuAl₂ phase peaks, the peaks corresponding to Al₂O₃ are indexed. Further, JCPDS no. 89-4037 (α -Al) and JCPDS no. 25-12 (β -CuAl₂) confirmed the diffraction peaks of the alloy. The peaks of Al₂O₃ were also verified by JCPDS no. 10-173. In the XRD pattern of nanocomposites, no further peaks of any intermetallic phase can be seen. This implies that no new phase was formed because of the reaction between the aluminium matrix and the Al₂O₃ reinforcement and that alumina is thermally stable in the matrix. This is in line with the observation reported elsewhere [41].

3.3 Hardness of materials

Figure 9 shows the Vickers microhardness values of the fabricated materials. As shown in the figure, the hardness of the unreinforced alloy is 122 VHN. The hardness of nanocomposites is between 142 and 150 at various percentages of Al₂O₃. The addition of Al₂O₃ nanoparticles up to 2 wt% increased the hardness up to 150 VHN. This was due to the uniform distribution of particles on the matrix alloy. The addition of hard nanoparticles strengthened the base matrix and helped in load sharing. Al₂O₃ nanoparticles in the base Al matrix act as barriers and restrict dislocation motion in the matrix [41]. On the other hand, the further addition of alumina nanoparticles reduced the hardness. As the number of nanoparticles added increases, the reinforcement agglomerates, reducing the hardness [42].

3.4 Analysis on tribocorrosion behaviour

3.4.1 Co-efficient of friction and open-circuit polarization (OCP)

Figure 10a–d shows the coefficients of friction (COF) and OCP of alloy and nanocomposites during tribocorrosion at different exposure times. The sliding times were 240, 300, 600, and 900 s. During the test, the material was initially left for some time to stabilize. The figure shows that, at the beginning of sliding, the OCP value shifts sharply to the negative side due to cathodic shift and then pauses at a potential value. By accelerating the anodic reaction, the metal surface developed naturally inside the wear track was destroyed, and a new metal surface was revealed. As a result, the discharge of electrons polarized the surrounding region.

Fig. 7 Microstructure of materials: **a** SEM image of AA2014 and **b, e** HR-SEM images of AA2014/ Al_2O_3 nanocomposites

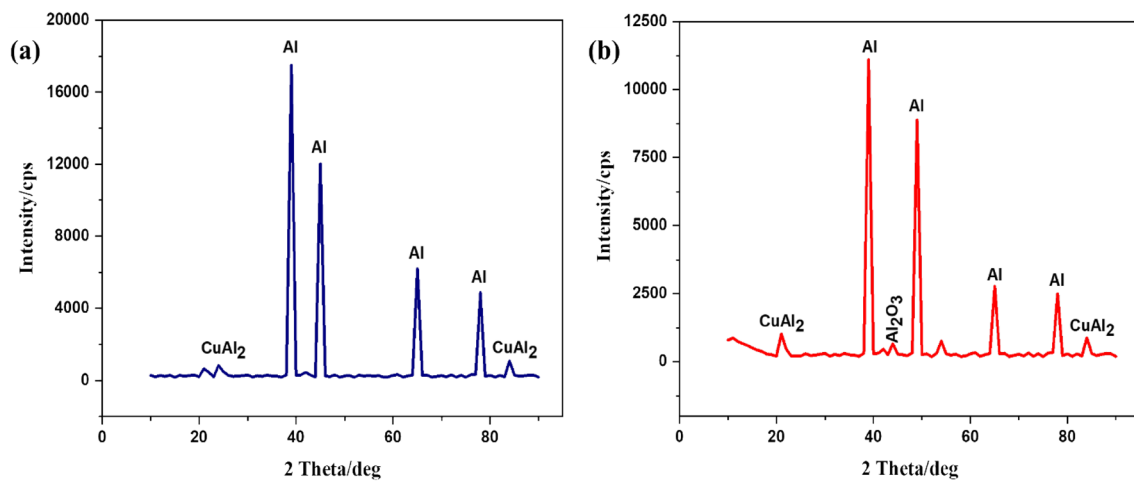
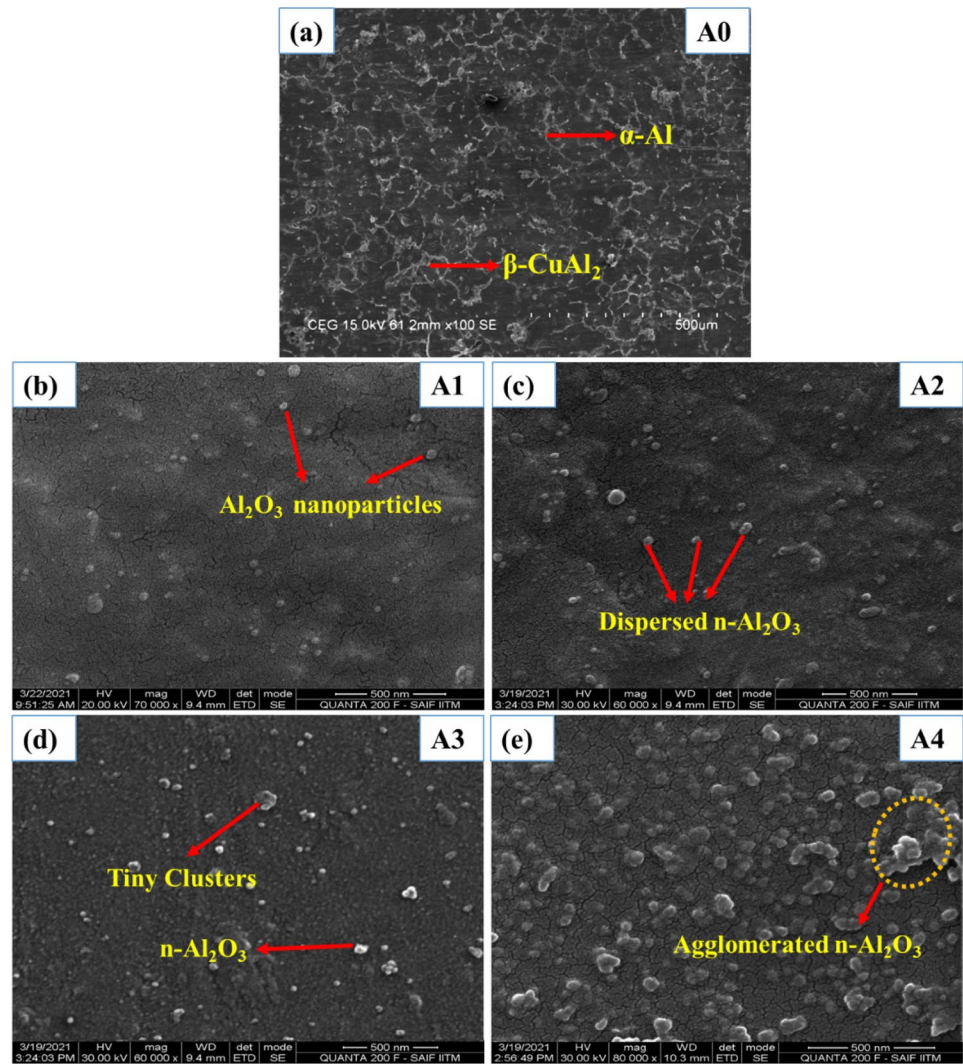


Fig. 8 XRD pattern of materials: **a** alloy and **b** nanocomposite

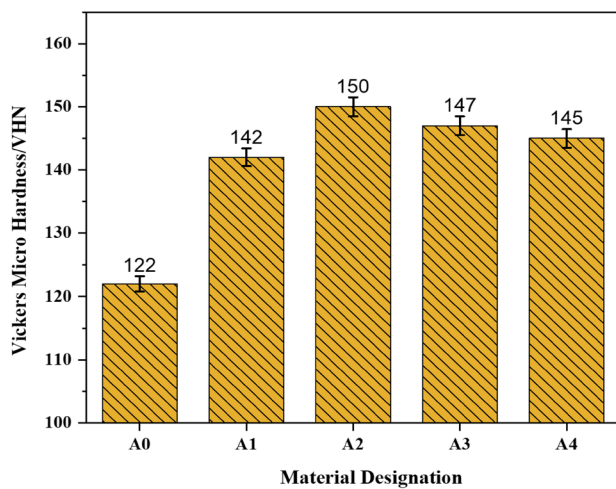


Fig. 9 Vickers microhardness of alloy and nanocomposites

Following the end of sliding, the OCP value increased only a little due to the reassignment of the passive state in the track area. The cathodic shift in OCP was achieved in this

test due to electrochemical re-passivation. When exposed, the de-passivated area corrodes at a higher rate until another passive film forms which is known as re-passivation. However, mechanical de-passivation was observed in a variety of nanocomposites over a range of sliding times [43, 44].

When materials were exposed to a 600-s initial exposure, specimen A0 started to deteriorate at a higher level. As demonstrated in Fig. 10a, this was attributable to the abrupt attack of chloride ions and the absence of reinforcement in the matrix. A higher OCP of -0.8 to -0.9 V with a COF of 0.35 was found for A0. At all sliding times, the electrode potential of aluminium alloy was substantially higher than that of composites, resulting in larger worn surfaces due to poor hardness and weaker corrosive resistance [28]. The inclusion of alumina nanoparticles improved the COF and OCP in nanocomposites. Because of the addition of alumina, the OCP of nanocomposites A1 shifted toward positive potential with a lower COF. Similarly, the inclusion of reinforcement increased the positive potential of A2 and A3 throughout all exposure conditions. It is evident that A3 outperformed the other nanocomposites. In A3, the

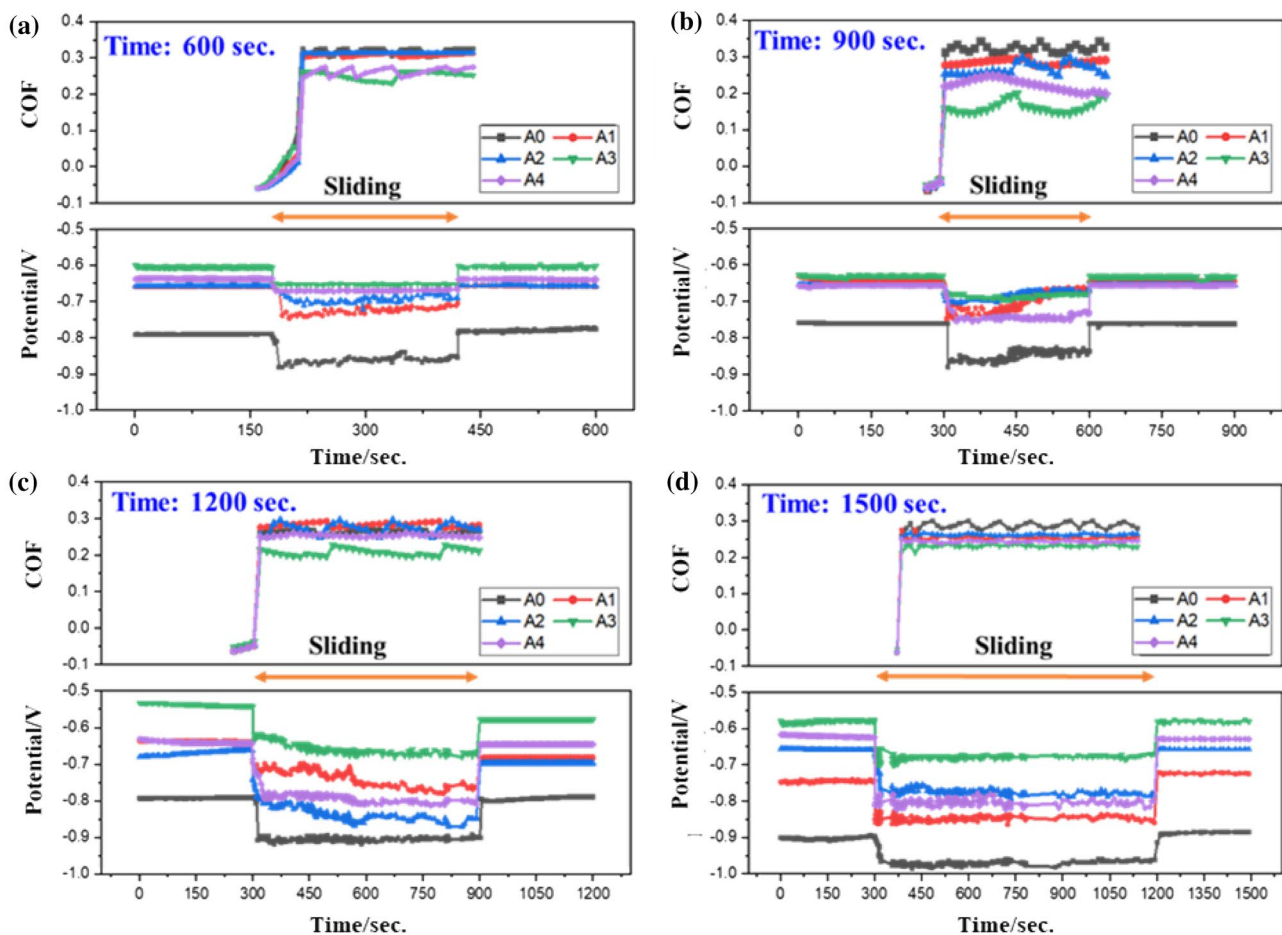


Fig. 10 COF and OCP of tribocorrosion samples at various exposure times **a** 600, **b** 900, **c** 1200, and **d** 1500 s

reinforcement strengthened the surface and decreased the OCP to -0.6 V with a COF of 0.28 as shown in Fig. 10a.

Furthermore, the addition of more reinforcement caused agglomeration, which increased grain size and lowered hardness in nanocomposite A4. The clustered particles in A4 increased the observed negative potential from -0.6 to -0.8 V, with a COF ranging from 0.20 to 0.25 at all exposure levels. Because of the presence of CuAl_2 , the increase in the stabilization period has a propensity to stabilize the oxidation process. The stabilized alumina hydroxide layer produced on composites exhibits little negative potential at 900 s as shown in Fig. 10b. The highest positive potential ranged from -0.62 to -0.68 V, with a COF of 0.15 to 0.20, in A3. Because of the initial cracks on the surface, unstable COF occurred at the beginning. The COF in nanocomposites was higher for a while and subsequently reduced due to the robust protective layer. At exposure times of 1200 and 1500 s, as shown in Fig. 10c and d, the circuit polarization

ranged from -0.9 to -1.0 V and the COF ranged from 0.3 to 0.35. The thick oxide layer was degraded due to excessive chloride ions and mechanical wear due to longer exposure times of 1200 and 1500 s. In comparison, it is worth noting that the composite containing 3 wt% Al_2O_3 exhibited good corrosion resistance and greater wear track re-passivation.

3.4.2 Electrochemical impedance spectroscopy

The impedance curves of the specimens after different sliding periods were recorded in a static state are depicted in Fig. 11a–d. The impedance curves of all of the specimens are semi-circles of varying diameters. In curves, the x -axis represents actual impedance and the y -axis represents imaginary impedance. In general, the larger the diameter of the semi-circle, the stronger the corrosion resistance. Furthermore, it depicts the occurrence of charge transfer provided by metallic atoms (Al) that get ionized when in contact with

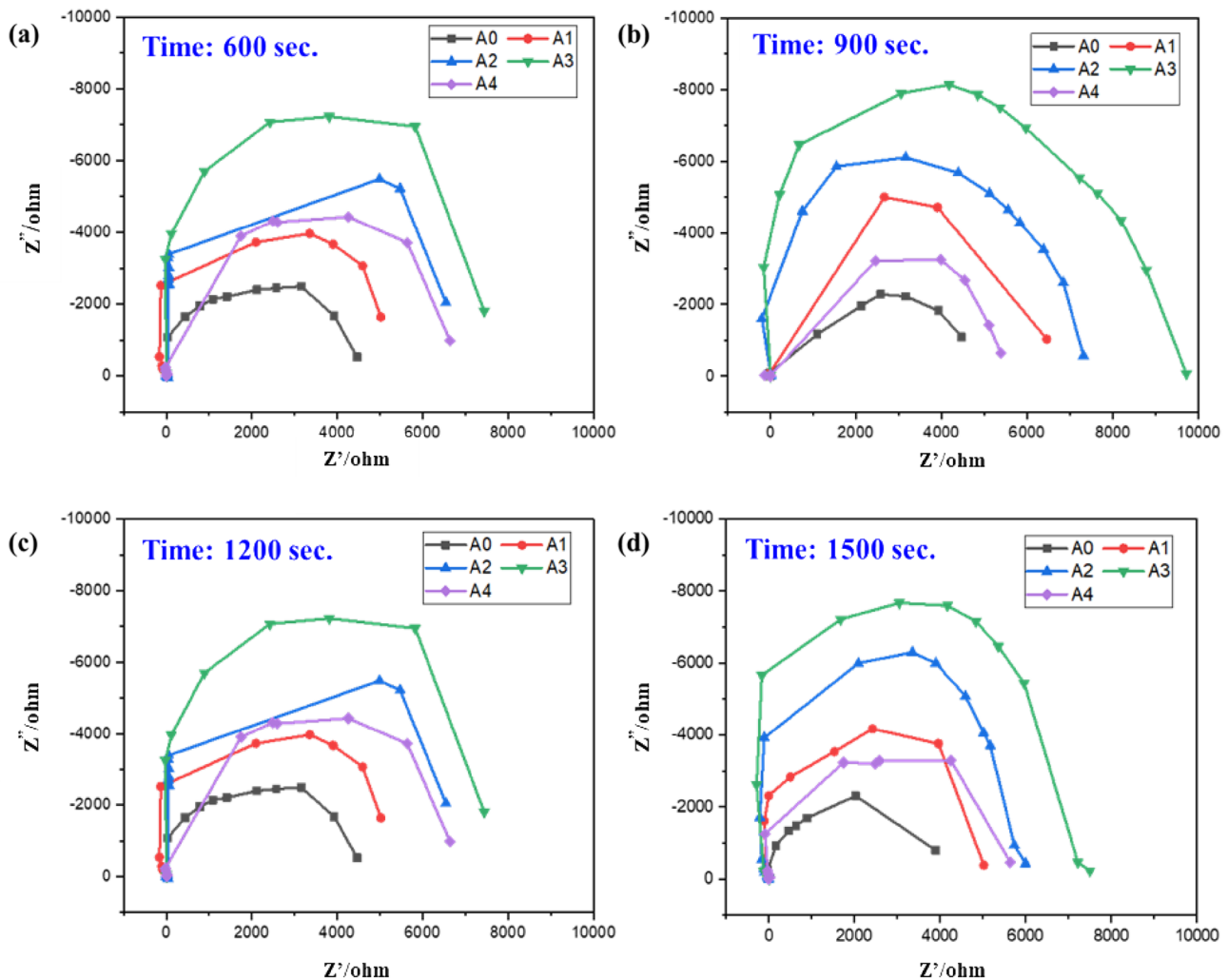


Fig. 11 Nyquist plot of tribocorrosion samples at a various exposure time **a** 600, **b** 900, **c** 1200, and **d** 1500 s

an electrolytic (NaCl) solution [45]. According to Fig. 11a, the resistance of unreinforced alloy was lower than that of nanocomposites, due to the absence of reinforcement. At 600 s, the resistance of the materials gradually increased in nanocomposites A1, A2 and A3 due to constant addition of Al_2O_3 nanoparticles. Furthermore, the addition of a large amount of reinforcement resulted in a clustered structure that increased grain size while decreasing the semi-circle in nanocomposite A4 seen in all exposure times.

At 900 s, A3 exhibited the highest impedance level due to uniformly dispersed reinforcement on the substrate. The presence of passive films on the surface minimizes corrosion and surface defects, as indicated by larger curves [28]. The highest impedance level was seen in Fig. 11b due formation of an alumina oxide layer on the surface enhanced the resistance of materials to corrosion. The width of the curve increased due to the formation and accumulation of corrosion products. It further reduced with increasing the

exposure time due to the dissolution of oxide film at localized areas [46]. Further, the corrosion duration increased to 1200 and 1500 s, fractures the passive oxide layer accelerating the ion discharge resulting in reduced resistance as seen in Fig. 11c and d. As shown in Fig. 11b, A3 moved forward with a bigger diameter to indicate the polarization impedance, in which the corrosion rate was reduced in the order of $A3 < A2 < A4 < A1 < A0$.

3.4.3 Potentiodynamic polarization plot

Potentiodynamic polarization (PDP) curves of alloy and nanocomposites without sliding conditions measured in 3.5 wt% NaCl solution for varying sliding times are shown in Fig. 12a–d. The PDP curves are also known as Tafel plots. They are used to evaluate the corrosion resistance of a material. The cathodic curve is on the left side of the Tafel plot, while the anodic curve is on the right. The material suffers

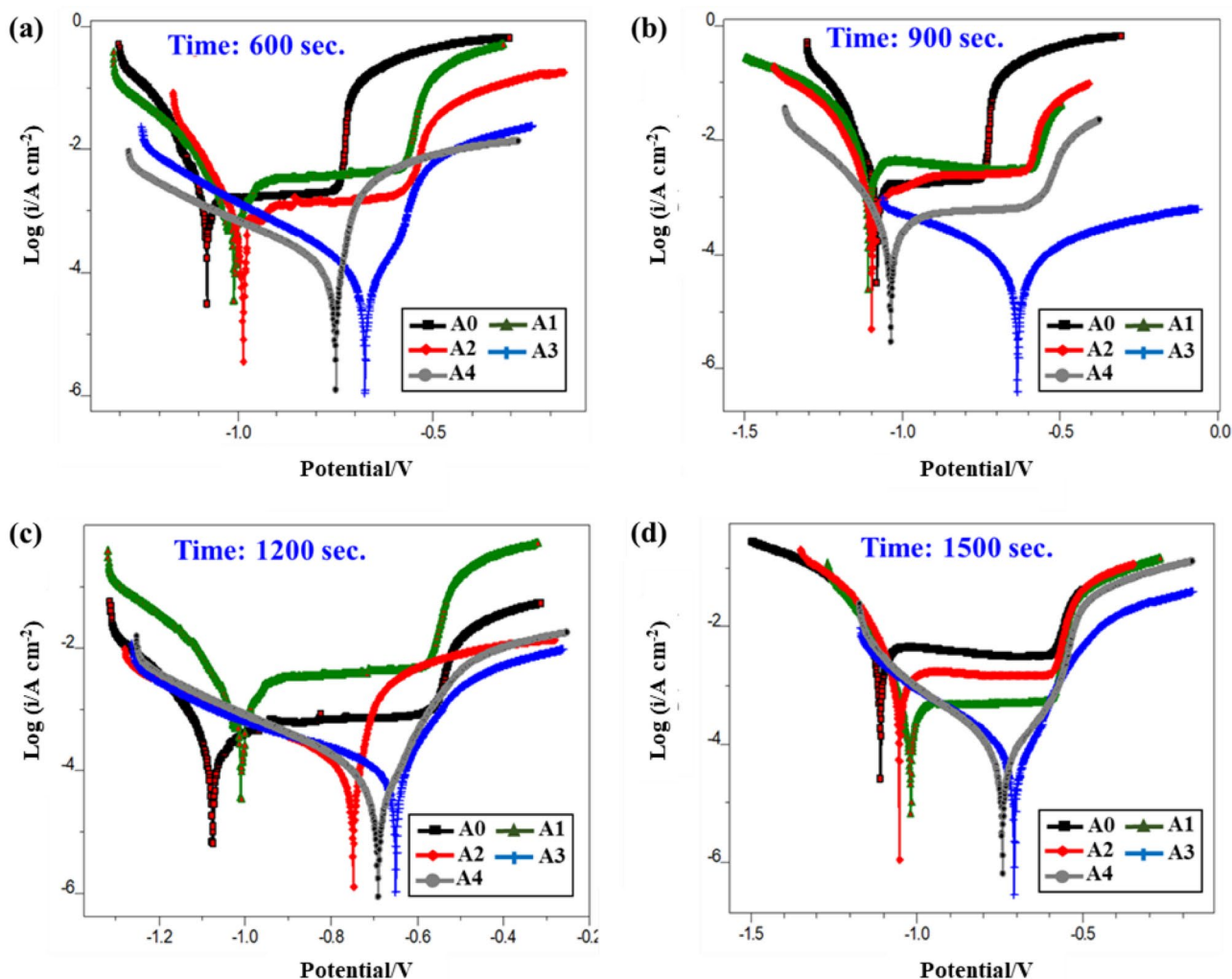


Fig. 12 Polarization curve of tribocorrosion samples at a various exposure time **a** 600, **b** 900, **c** 1200, and **d** 1500 s

severe chloride attack due to more Cl^- ions in the electrolyte during the initial stages of sliding at lower test durations [45]. As shown in Fig. 12a, alloy corrodes severely in static corrosive conditions with increased potential (E_{corr}) of -1.1 V, which corresponds to a corrosion current density of 9.086×10^{-4} . On the other hand, the nanocomposites A1 to A4 exhibit minimal potential from -0.690 to -1.02 V where the A3 had the lowest potential of -0.690 V. In Fig. 12b, the re-passivation process lowers current density with higher potential on nanocomposites, notably on A3, which is opposite to A0. The wear-induced method degrades the protecting alumina hydroxide layer by increasing the exposure period. It lowers the corrosion potential of alloy and nanocomposites with higher current density, as illustrated in Fig. 12c and d.

It is clear that the corrosion resistance of unreinforced alloy and nanocomposites was lower than that of A3. Because of the presence of high alumina particles, the nanocomposite A3 demonstrated excellent corrosion resistance, with current densities ranging from -0.6 to -0.8 V at different corrosion times. However, further increasing the test duration, the protective layer of materials fractures during sliding, allowing corrosion ions to infiltrate the substance and generate corrosion pits and fractures on the material's surface [47, 48]. Generally, polarization curves are attributed to aluminium dissolution to form Al^{3+} which indicates the dissolved oxygen to form Eqs. (3 and 4) [49, 50].



Then, Al^{3+} reacts with OH^- to form aluminium hydroxide on the surface shown in Eq. (5 and 6).



Aluminium hydroxide changes gradually to aluminium oxide, resulting in the formation of passive films.



The E_{corr} and I_{corr} values of alloy and nanocomposites are tabulated in Table 5. It indicates that the addition of Al_2O_3

particles decreased the current density (A cm^{-2}) and corrosion potential (V). The higher the E_{corr} value, the larger the anodic current density. At lower exposure times, A0-induced more oxidation over the natural layer, resulting in increased corrosion rate. But the nanocomposites had lower E_{corr} and I_{corr} due to the uniform distribution of alumina. A3 had minimal values at 600 s. When tested for corrosion resistance for 900 s, the A3 sample outperformed the other specimens. This indicates the incremented resistivity in A3 nanocomposite. The corrosion potential, which is directly proportional to current density in all corrosion exposures, was reduced in the initial stages [28]. The addition of nanoparticles effectively enhanced the resistance which showed a decrease in its polarization current, dimensions of erosion track and coefficient of friction. [30]. Furthermore, at higher exposure time of 1200 and 1500 s, the higher dissolution of ions and sliding action formed pitting on the surface which reduces the corrosion resistivity.

The cyclic potentiodynamic polarization (CPP) curves for alloy and nanocomposites tested for 900 s are shown in Fig. 13. The figure shows that the corrosion potential of the forward scan is better than the corrosion potential of the backward scan. According to reports, if forward corrosion potential is higher than backward corrosion potential,

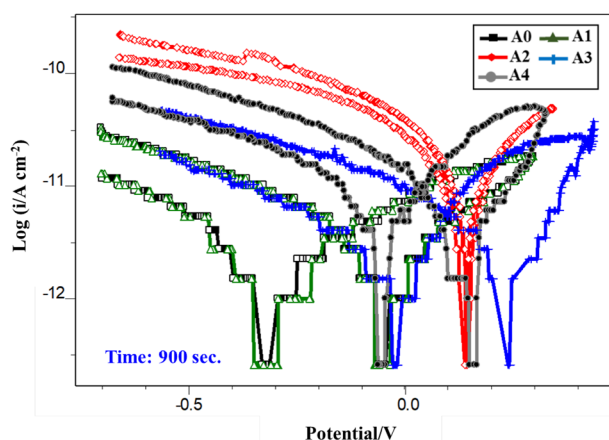


Fig. 13 Cyclic potentiodynamic polarization curves of samples tested at 900 s

Table 5 E_{corr} and I_{corr} values of tribocorrosion samples at various exposure times

Exposure time (S)	600		900		1200		1500	
	E_{corr} (V)	I_{corr} (A cm^{-2})	E_{corr} (V)	I_{corr} (A cm^{-2})	E_{corr} (V)	I_{corr} (A cm^{-2})	E_{corr} (V)	I_{corr} (A cm^{-2})
A0	-1.099	9.086×10^{-4}	-1.101	7.956×10^{-4}	-1.104	8.012×10^{-4}	-1.124	9.242×10^{-4}
A1	-1.011	7.845×10^{-4}	-1.103	7.112×10^{-4}	-1.030	7.702×10^{-4}	-1.057	7.814×10^{-4}
A2	-0.988	6.081×10^{-4}	-1.101	5.932×10^{-4}	-1.049	6.115×10^{-4}	-1.009	6.159×10^{-4}
A3	-0.689	5.212×10^{-4}	-0.621	4.889×10^{-4}	-0.645	5.230×10^{-4}	-0.701	5.876×10^{-4}
A4	-0.645	6.005×10^{-4}	-1.035	5.970×10^{-4}	-0.712	5.971×10^{-4}	-0.758	6.011×10^{-4}

the passive film on the metal surface will be more resistant [45]. Thus, the samples are not susceptible to repassivation under these conditions. According to the CPP curves, partial passivation occurred in the forward anodic scan when the potential was highly negative compared to the specimen at ideal corrosion potential [27]. Following that, a significant increase in anodic current was occurred as a result of uniform pit growth or pit propagation. Nevertheless, because there was no stable passive film on the alloy, it was concluded that repassivation occurred at the backward scan and the damaged film restored. Another reason for the more negative backward corrosion is the possibility of the corroded portions acting as anodic zones, causing the corrosion to begin [27].

The corrosion rate of materials exposed to tribocorrosion tests at various exposure times is depicted in Fig. 14. At all exposure times, the absence of alumina oxide reinforcement significantly increased the tribocorrosion rate of A0. At an initial corrosion time of 600 s, the material subjected to severe chloride attack accelerates corrosion owing to intermetallic layer breakdown. The inclusion of alumina up to 3 wt% increased the corrosion resistance of composites A1, A2, and A3. Due to the uniform distribution of hard ceramic particles throughout the surface, the composite A3 clearly outperforms other materials in terms of corrosion resistance. Furthermore, the presence of clustered nanoparticles increased the corrosion rate in A4 substantially throughout all exposure periods.

At 900 s, the ions dissolved in the electrolyte reaches the alumina surface, limiting corrosion where pure alloy takes the greater decay owing to reduced hardness. It was determined that a larger alumina addition generated a persistent protective layer, which reduced corrosion in A3 at 900 s. Moreover, the insoluble corrosion products restricted the movement of ions on the surface

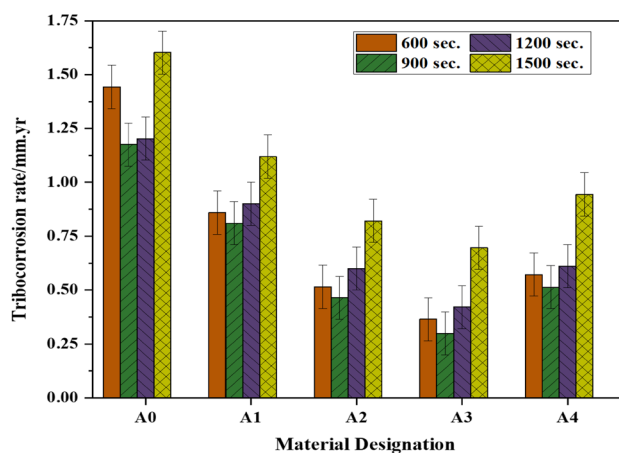


Fig. 14 The corrosion rate of tribocorrosion specimens at various exposure times

which reduces the corrosion rate. Similarly, the corrosion rate of materials increased with increasing exposure times of 1200 s due to a damaged aluminium hydroxide layer ($\text{Al}(\text{OH})_3$) during sliding. This was due to the higher exposure time of 1500 s, at which, the film destroyed by Cl_2 in the solution. Thus, the localized pitting corrosion took place on the surface. Figure 15a–t depicts the corroded surface of tribocorrosion samples tested at various exposure durations.

The mechanism of wear-induced corrosion occurs primarily as a consequence of (i) mechanical wear, which accelerates material deterioration and degrades the protective layer; (ii) higher plastic deformation in the wear track, which results in greater corrosion and (iii) increased wear causes increased ion dissolution, which leads to increased corrosion [27]. The wear mechanism of the specimens was majorly abrasion and plastic deformation. These processes occurred along with pitting corrosion mechanism on the surface of the alloy [47, 48]. Mechanical wear was reduced when specimens were exposed to a tribocorrosion test for 900 s. The surface of the materials after tribocorrosion test was examined using optical images (Fig. 16a–e) and SEM images (Fig. 16f–j). The worn and unworn surfaces of AA2014 alloy are shown in Fig. 16a, indicating that the alloy was extremely rough. More pronounced scars and parallel furrows visible in alloy demonstrate the material's volume loss [50]. Figure 16f, the SEM image of alloy reveals a crater with micro-cracks on the worn surface caused by the inadequate hardness of the alloy.

The morphologies of the worn surface were smoother in composites due to the inclusion of Al_2O_3 particles, as seen in Fig. 16b–e. In inferior surfaces, grooves, fragments, and micro-cracks appeared. While increasing the alumina concentration, fewer craters and scratches suggest reduced volume loss in composites as observed in SEM in Fig. 16g–j. When reinforcement was increased to 3 wt%, cracks and pits were greatly reduced, resulting in less volume loss with a lower COF [26]. In terms of corrosion rate, the composite A3 has superior resistance to 3.5 wt% NaCl solution in tribocorrosion, as shown in Fig. 16d and i. The corroded surface of nanocomposites tested at different exposure times are shown in Fig. 17a–d (OM images) and e–h (SEM images). All figures depict the presence of pitting corrosion. From Fig. 17a, it can be observed that at the initial stages, the surface was severely attacked by chloride ions forming higher corrosion. Further, at 900 s the composite reveals reduced corrosion pits and debris on the surface, as shown in Fig. 17b. The fragmented layer formed on the track area is shown in Fig. 17f.

The deterioration process of the fragmented layer can be categorized into four divisions: (1) Large fragments form in the wear track area at high potentials. (2) Under sliding action, cracks formed in the fragments after a single

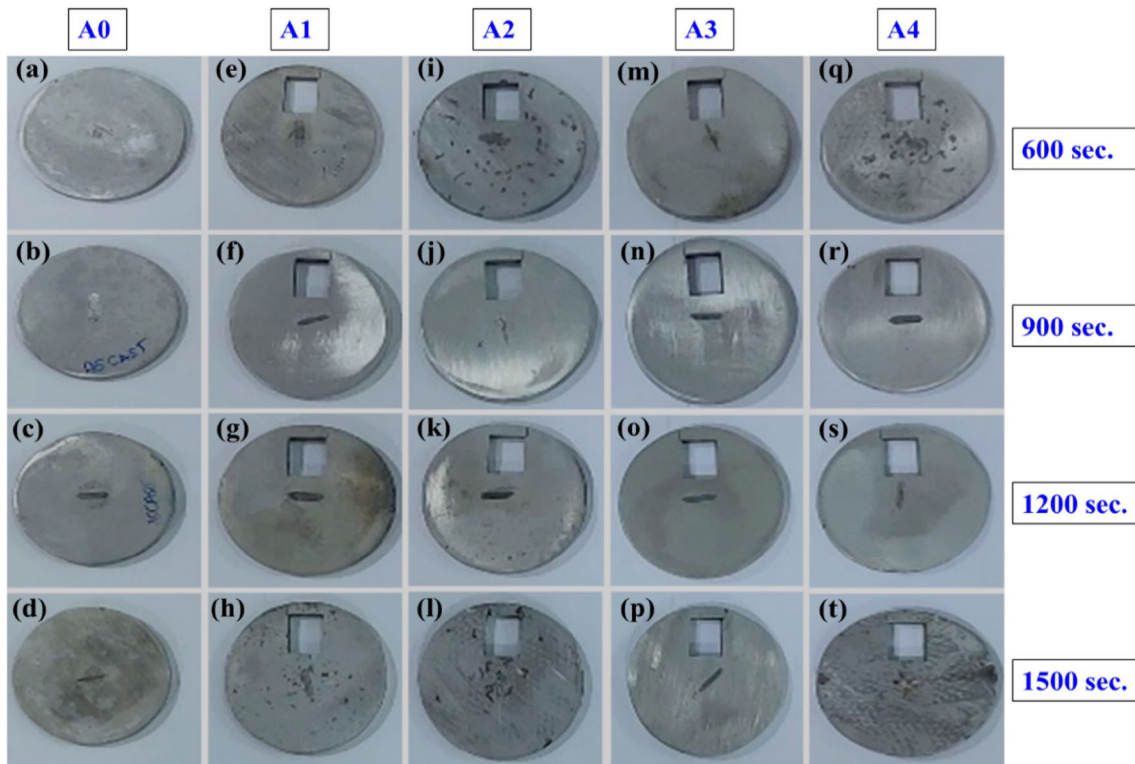


Fig. 15 a–t The corroded surface morphology of tribocorrosion samples

or multiple numbers of sliding. (3) The fragments are subdivided into small fragments. (4) Micro fragments are removed to form wear debris due to the action of friction and ion dissolution [30]. Material wears was expected to increase with applied potential because of the more visible pits formed in the wear track at high exposure, as seen in Fig. 17g. Moreover, the existence of corrosion pits reduced the in-time area contact, resulting in mechanical wear on the track and formation of debris as seen in Fig. 17g.

3.5 Electrochemical corrosion analysis

3.5.1 Open-circuit polarization

Open-circuit polarization curves are commonly used to study qualitatively the corrosion behavior of materials. The OCP curves of alloy and nanocomposites measured in 3.5 wt% NaCl arrangement, subjected to different corrosion periods is presented in Fig. 18a–d. The nanocomposite A3 has the lowest potential throughout all exposure periods. The inclusion of evenly dispersed Al_2O_3 nanoparticles was responsible for this. On the other hand, the reinforcements in the nanocomposite A4 developed clusters in the matrix, indicating increased corrosion potential at all exposure times. Because of the lack of reinforcement and breakdown of passive films, the highest potential was found in A0. During

the first 600 s, the OCP value of alloy and nanocomposites shifted to the positive potential direction. As shown in Fig. 18a, the highest negative potential found in A0 varies from -0.750 to -0.775 V. In the case of A1, A2 and A3 nanocomposites, a positive potential movement in OCP can be observed. This was due to the addition of alumina particles. However, the lowest potential was obtained for A3 nanocomposite, ranging -0.650 to -0.700 V. The solubility of Al^{3+} enhances dissolution, promotes chloride attack, and oxidizes the materials, increasing their corrosion potential [51]. While increasing the exposure period to 900 s, unstable OCP data were recorded in the range -0.675 to -0.875 V, as shown in Fig. 18b. That was due to compound dissolution and the increased number of OH^- ions constantly diminishing the oxide film [52].

As the exposure time was increased to 1200 s, the least potential values were found to be between -0.575 and -0.825 V as shown in Fig. 18c. This was primarily due to the reduction of water, which resulted in the formation of protective aluminium hydroxide ($\text{Al}(\text{OH})_3$), which lowers the corrosion rate of materials at higher exposure levels [53]. As depicted in Fig. 18d, at an exposure period of 1500 s, the potential dropped sharply in the negative direction from -0.65 to -0.835 V. This indicates increased corrosion as a result of the constant attack of chloride ions on the surface. The electrons on the cathode end react with

Fig. 16 Microstructure of tribo-corroded samples at 900 s **a–e** OM images and **f–j** SEM images

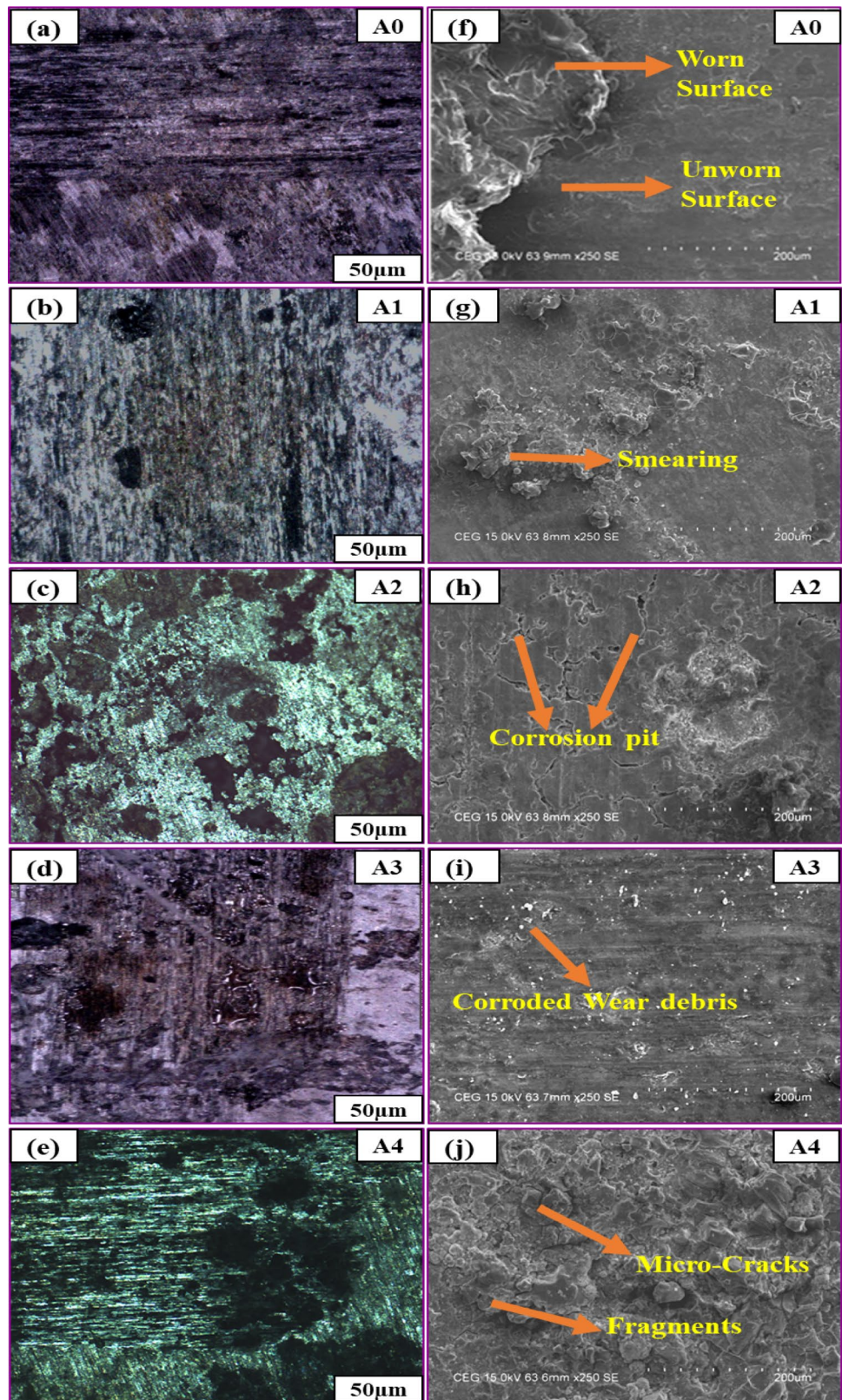
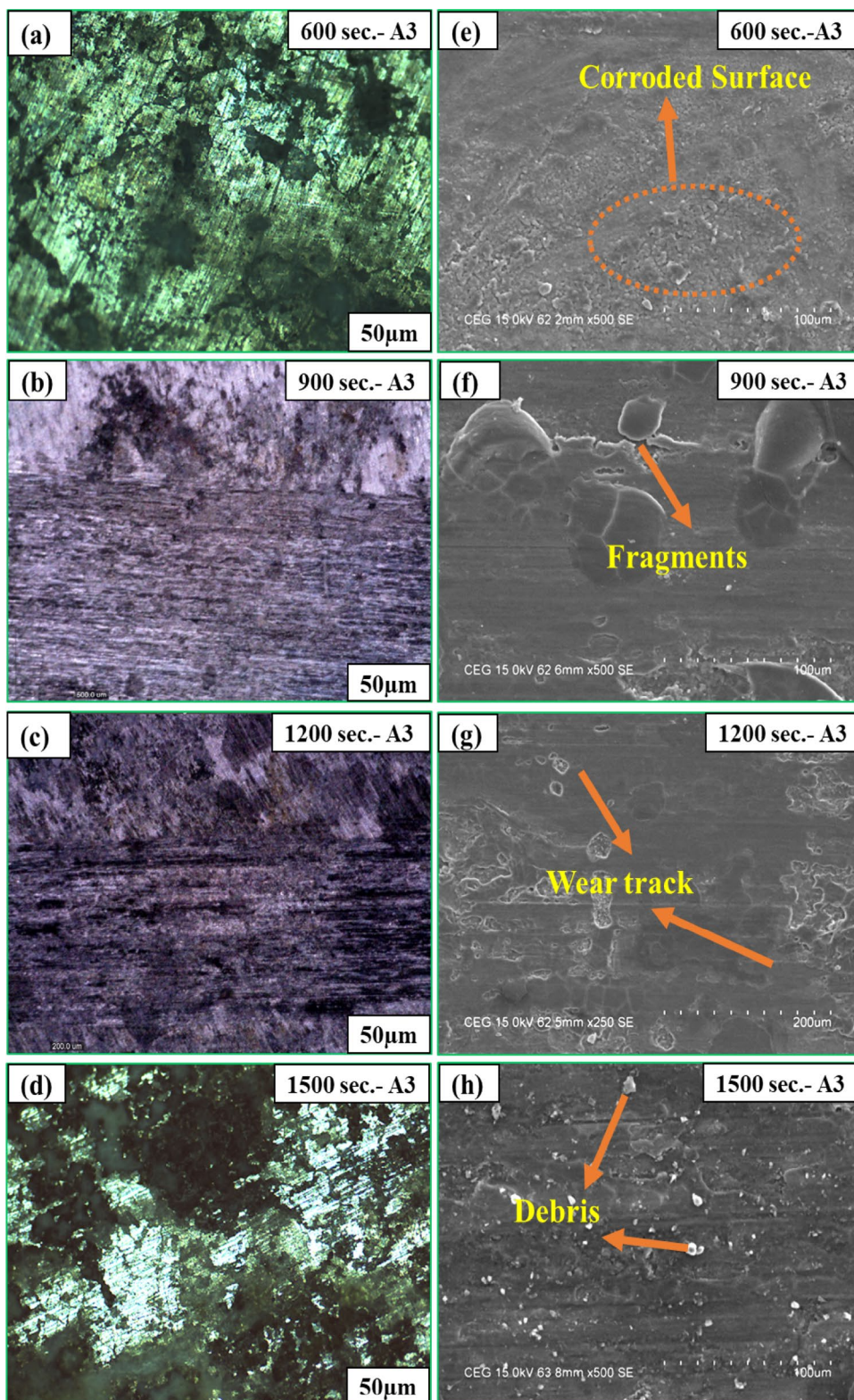


Fig. 17 a, b OM images and c, d SEM images of tribo-corroded sample A3 at different exposure times



water as a result of the electrolytic solution, causing each water molecule to release one hydrogen particle. Aluminium reacts with oxygen and aqueous solutions to form the passive

film of Al_2O_3 . It arises as a result of the reaction described in Eqs. (7) and (8).

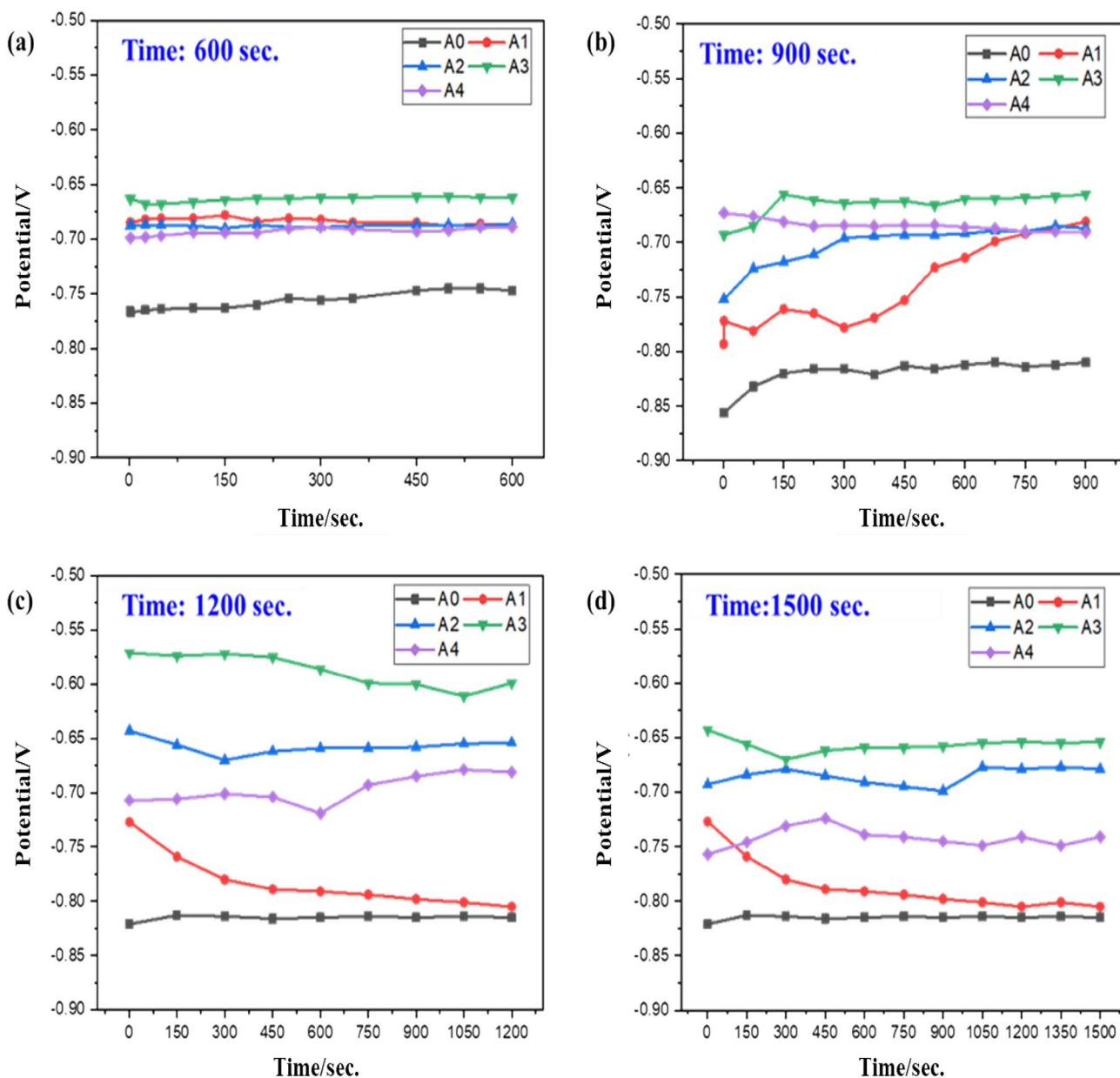
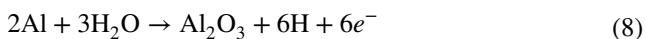
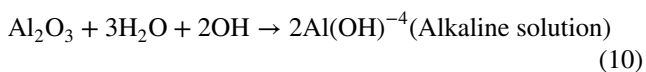
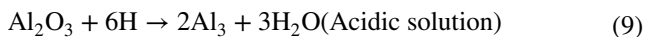


Fig. 18 Open-circuit potential of electrochemical samples at various exposure times **a** 600, **b** 900, **c** 1200 and **d** 1500 s



The oxide film disintegrates in both acidic and high alkalinity conditions [51], as indicated in Eqs. (9 and 10).



Thus, the passive alumina layer produced over the surface prevents the removal of ions that stabilize the materials in 1200 s. Bonding between the matrix and reinforcement was disrupted due to prolonged exposure at 1500 s. Besides, increased corrosion occurred as a result of the deterioration of the protective alumina layer.

3.5.2 Electrochemical impedance spectroscopy

The electrochemical impedance spectroscopy curves of alloy and nanocomposites investigated at different exposure times are shown in Fig. 19a–d. The figure represents

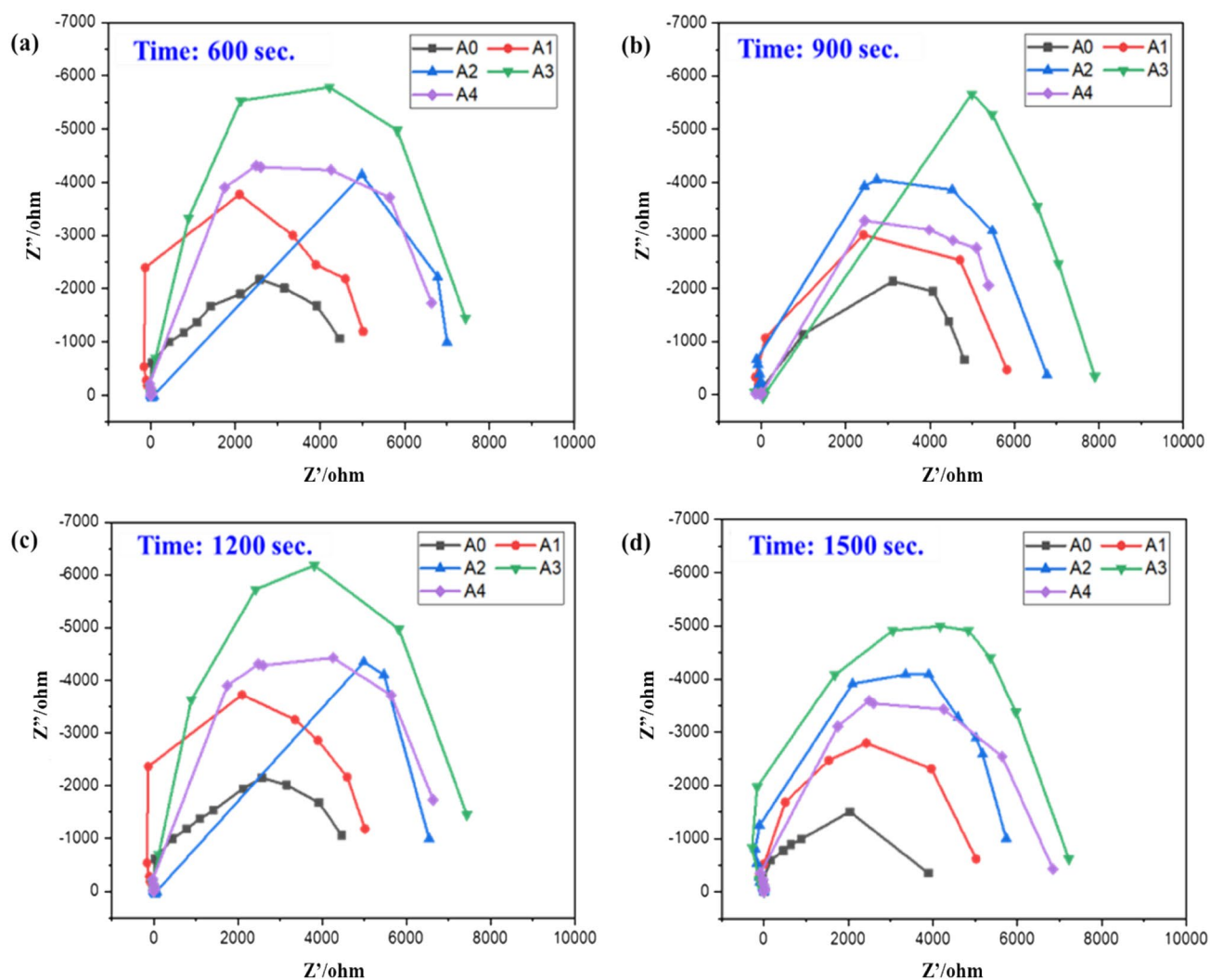


Fig. 19 Nyquist plot of electrochemical samples at various exposure time **a** 600, **b** 900, **c** 1200 and **d** 1500 s

the impedance level while electrons were transported to the material. A larger curve, suggests a higher impedance with less corrosion. At 600 s, the impedance was measured, and the unreinforced alloy exhibited a lower capacitive curve diameter than reinforced composites, as illustrated in Fig. 19a. As the weight percent of reinforcement increases, the diameter of the capacitive curves seems to increase in nanocomposites A1 to A3 [28]. On the other hand, higher concentrations of alumina nanoparticles caused agglomeration, reducing the corrosion resistance of the nanocomposite A4 at all exposure times. Furthermore, extending the exposure period to 900 and 1200 s tends to stabilize the oxidation reaction, resulting in reduced corrosion, as seen in Fig. 19b and c.

The nanocomposite A3 was more corrosion resistant due to the inclusion of hard ceramics. Because ion exchange is required to sustain corrosion, it may deduce that resistivity is dependent on time and wt% of reinforcements [33].

Therefore, composite A3 proceeds with a larger diameter indicate the polarization impedance. As a result, composite A3 progressed with a larger diameter to represent the polarization impedance. Because of the longer exposure times, the ions on the metal surface dissolved more rapidly. At 1500 s, this accelerated the corrosion on alloy and nanocomposites, as illustrated in Fig. 19d. As indicated Fig. 19, the corrosion rate was in the sequence $A3 < A2 < A4 < A1 < A0$.

The Bode graphs of electrochemical impedance at 600, 900, 1200, and 1500 s are shown in Fig. 20. At low and mid frequencies, the phase angle values of all samples were between -50° and 50° , which was the optimal surface. The response of the electrolyte resistance is shown by constant $|Z|$ values near 0° for frequencies of 4 to -1 Hz. The corrosion resistivity of alloy and nanocomposites exposed for 1200 s was improved, with a near-phase value. A similar observation is reported elsewhere [43]. A wide phase angle peak was obtained from phase angle transference as shown

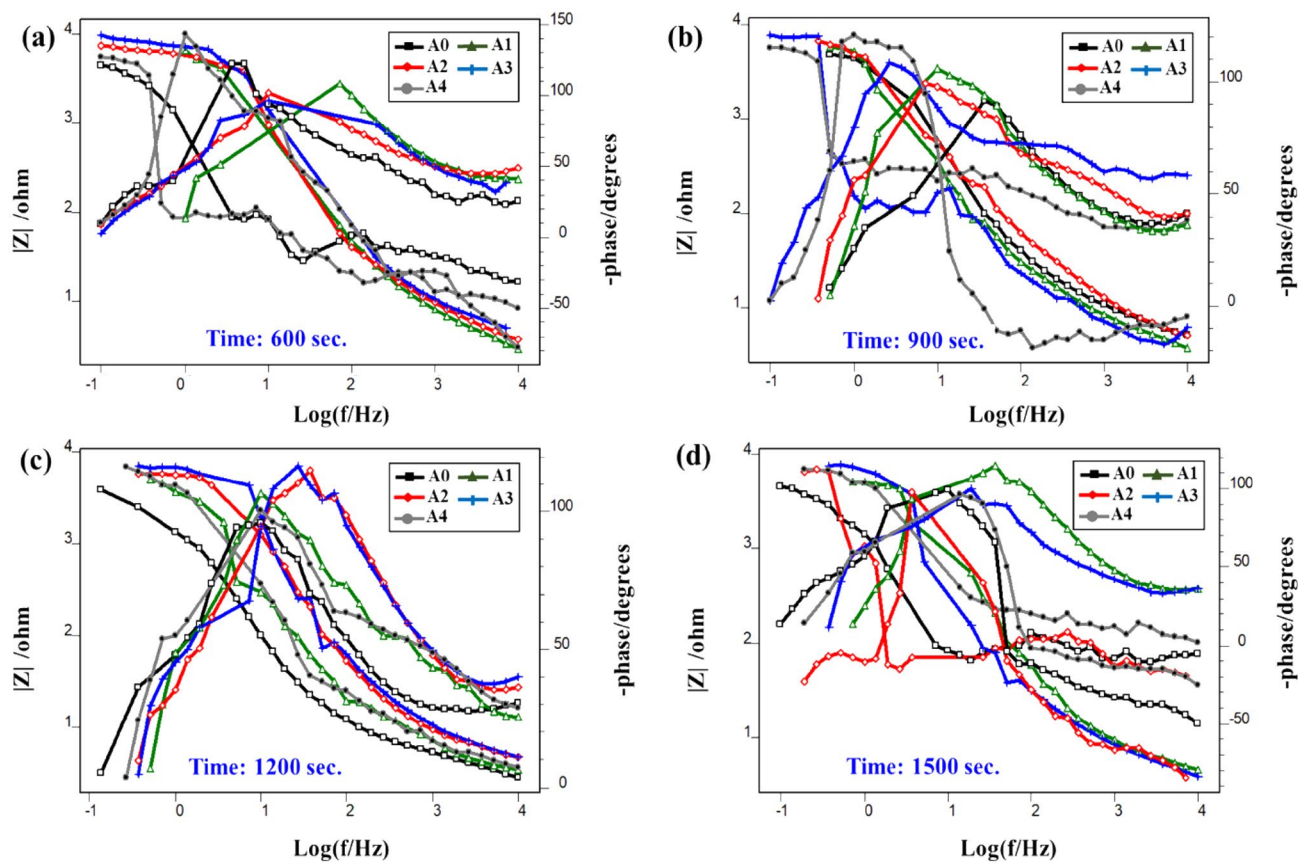


Fig. 20 Bode plot of electrochemical samples at different exposure times **a** 600, **b** 900, **c** 1200, and **d** 1500 s

in Fig. 20a and d. At higher frequencies (4 kHz), a large phase angle shift was observed in the case of the unreinforced specimen. At higher frequencies, nanocomposites, on the other hand, showed a high stable protective barrier. At 1200 s, the A3 displayed a widespread stable barrier throughout a wider frequency range.

3.5.3 Potentiodynamic polarization plot

The PDP curve for alloy and nanocomposites evaluated in static NaCl solution is shown in Fig. 21a–d. PDP curves are mainly composed of a cathodic region and an anodic region. The cathodic area indicates hydrogen evolution, whereas the anodic region indicates aluminium dissolution. Graphs show that deflected curves were generated at all exposure levels. When contrasted to nanocomposites, alloy corroded severely. This was due to poor hardness and severe chloride attack with high E_{corr} (-1.1123) and I_{corr} (5.086×10^{-5}). Because of the presence of an oxide film on the surface, A3 nanocomposite exhibited a lowest E_{corr} (-0.7893) and an I_{corr} (2.112×10^{-5}) seen in Fig. 21a. The anodic bend of the materials clearly reveals a shift to increased current density and probable corrosion changes to more negative (dynamic)

in the early stages [54]. The formation of hydrogen reactions on the alloy and nanocomposite surface during the initial exposure of corrosion interaction significantly accelerates the corrosion rate by eliminating the corrosion product film. Increasing the exposure time to 900 the composite A3 had E_{corr} value and I_{corr} value of (-0.611) and (1.756×10^{-5}) which caused the electrolyte solution to stabilize and form hydroxide layers on the surface. Additionally, at 1200 s, the presence of nano oxide particles and hydroxide film lowered the corrosion rate. The metal ions removed from the surface limit the plastic deformation of the materials and delay the corrosion action seen in Fig. 21b and c. The results indicated composites reinforced with 3 wt% Al_2O_3 had a lower tendency to get corroded in NaCl solution over all periods as the corrosion potential decreases. Moreover, at 1200 s, the nanocomposite A3 exhibited the highest resistance, with E_{corr} value (-0.5999) and I_{corr} (1.521×10^{-5}). However, considerable corrosion can be shown in Fig. 21d at 1500 s. This was due to the fact that the established protective alumina layer tends to break, allowing the solution to spread across the surface and start the corrosive attack [55].

The equivalent circuit for A3 tested at 1200 s, is shown in Fig. 22. The equivalent circuit correlations of components

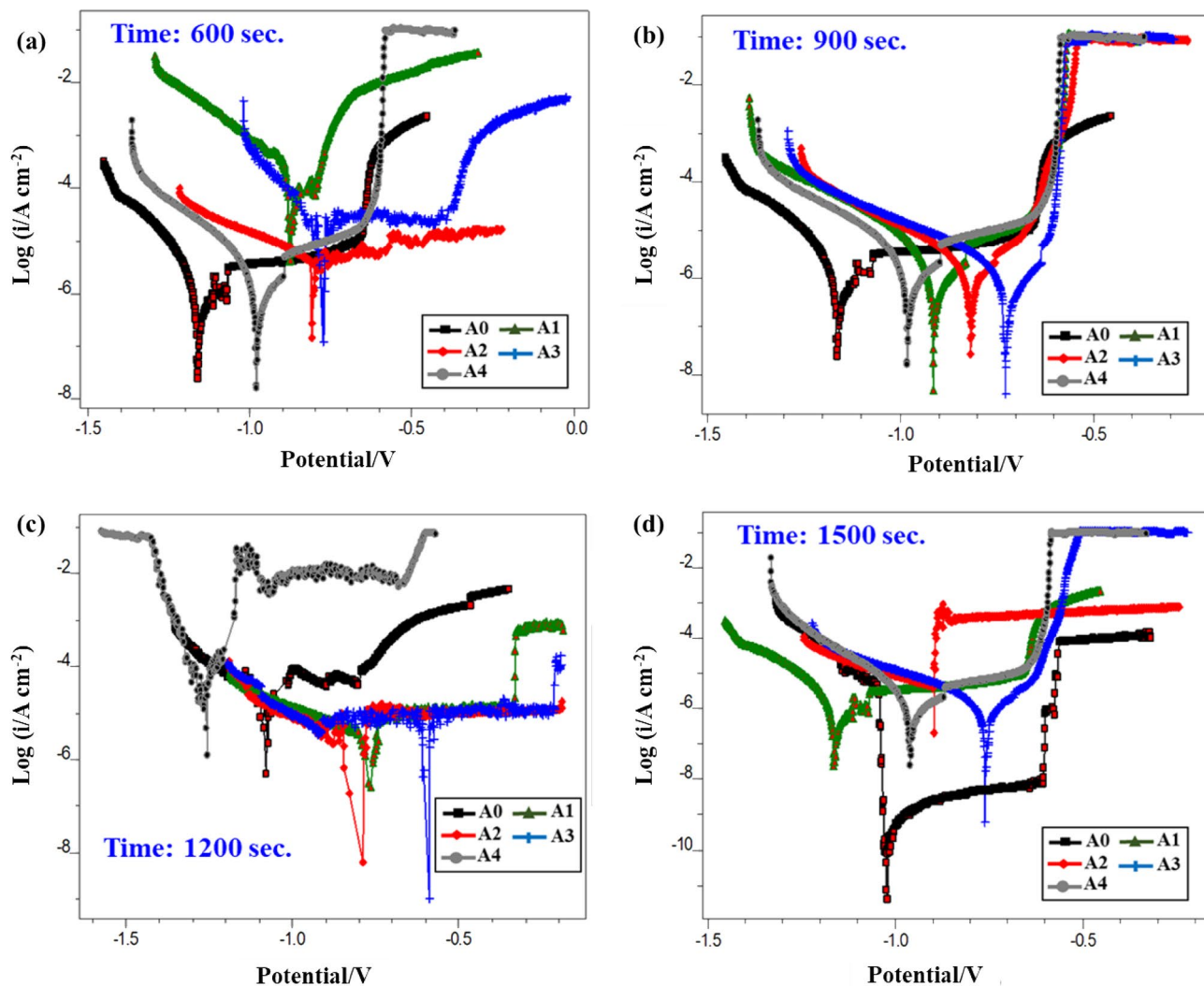


Fig. 21 Polarization curve of electrochemical samples at a various exposure time **a** 600, **b** 900, **c** 1200, and **d** 1500 s

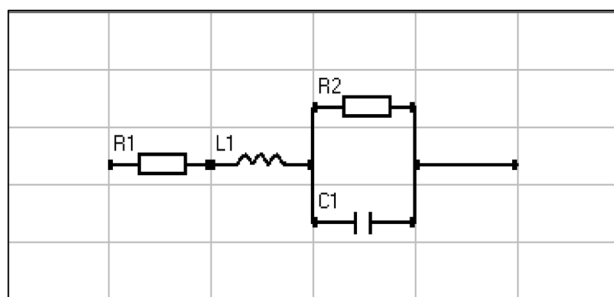


Fig. 22 The equivalent circuit for A3 at 1200 s

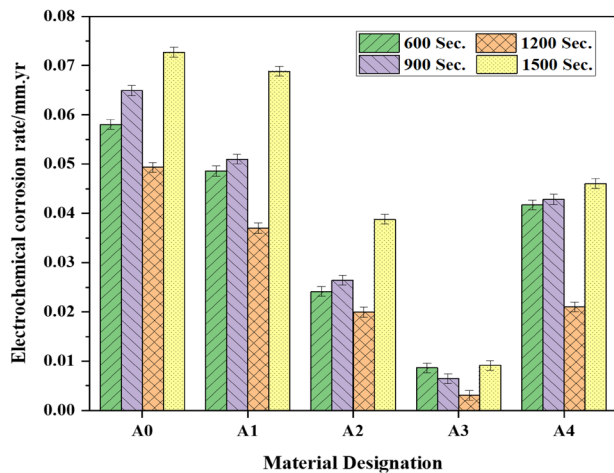
are: R_1 —charge transference resistance, R_2 —oxide layer resistance, L_1 —inductance, and C_1 —capacitance of circuit [23]. At 1200 s, the presence of a hard alumina layer in A3 reduced the formation of corrosion products on the surface.

The phase element present on the passive layer are responsible for potential transfer at constant interface. As a result, the constant phase elements present on the sample were used in the equivalent circuit model to determine capacitance and resistivity [43]. Table 6 shows the E_{corr} and I_{corr} values derived from equivalent circuit models using IVIUM software to measure corrosion potential.

Table 6 shows E_{corr} and I_{corr} values of specimens tested under various exposure conditions. A higher anodic current density is implied by a higher E_{corr} value. It increases oxidation and reduction, resulting in increased corrosion rate of A0 specimens. Because of the increased chloride attack at 600 s, the corrosion value tends to increase. The corrosion potential and current density were reduced when the exposure time was raised from 600 to 900 and 1200 s as shown in Table 6. According to the results, composite A3 treated at 1200 s had greater corrosion resistance. Because

Table 6 E_{corr} and I_{corr} values of electrochemical samples at various exposure times

Exposure time (s)	600		900		1200		1500	
Material designation	E_{corr} (V)	I_{corr} (A cm ⁻²)	E_{corr} (V)	I_{corr} (A cm ⁻²)	E_{corr} (V)	I_{corr} (A cm ⁻²)	E_{corr} (V)	I_{corr} (A cm ⁻²)
A0	-1.112	5.086×10^{-5}	-1.276	4.622×10^{-5}	-1.079	4.595×10^{-5}	-1.023	5.102×10^{-5}
A1	-1.104	3.719×10^{-5}	-0.912	2.811×10^{-5}	-0.740	2.694×10^{-5}	-1.178	3.811×10^{-5}
A2	-0.800	2.752×10^{-5}	-0.701	2.676×10^{-5}	-0.745	2.506×10^{-5}	-0.889	2.976×10^{-5}
A3	-0.789	2.112×10^{-5}	-0.611	1.756×10^{-5}	-0.599	1.521×10^{-5}	-0.779	2.456×10^{-5}
A4	-0.989	3.512×10^{-5}	-0.998	2.916×10^{-5}	-1.340	2.899×10^{-5}	-0.956	3.777×10^{-5}

**Fig. 23** The electrochemical corrosion rate of the alloys and nanocomposites

of the presence of Al_2O_3 nanoparticles in the grain precipitate zones, the aluminium nanocomposites disintegrate at the grain boundaries [55]. As a result, the presence of chloride ion in the dissolution reaction forms a protective hydroxide layer that strengthens the A3 substrate, resulting in lower corrosion values when compared to other composites.

The electrochemical corrosion rate of materials when exposed in 3.5 wt% NaCl solution is depicted in Fig. 23. According to a complex ion theory of corrosion, aggressive anions may substitute some oxide ion in the oxide film and form chemical reaction in the medium. Dissolution of the metal depends upon the relative stability of ions and the nature of anions. However, the less content of Al_2O_3 led to higher conductivity of the electrolyte solution. At lower exposure time, the corrosion attack deepened but at higher exposure time, the corrosion attack seems to be little widened. The reason for decreasing corrosion rate with increasing exposure time was the decrease in hydrogen evolution [56]. As indicated in the figure, at all exposure times, A0 was more prone to corrosion owing to a lack of reinforcement. Because the chloride concentration was greater during the initial stages of 600 and 900 s, the A0 corroded more quickly owing to the abrupt attack of chloride ions. The inclusion of

alumina nanoparticles decreased corrosion on A1. Further addition significantly decreased the corrosion rate of A2 and A3 nanocomposite. However, the inclusion 4 wt% of alumina nanoparticles resulted in a clustered structure, which lowered the resistivity of A4.

However, at 900 s, the consumption rate had increased slightly as a result of eroded items of enormous size. Owing to longer exposure time of 1200 s, the arrangement of the insoluble consumption items might also impede particle migration outside of the sample, lowering the electrochemical rate [55]. It was observed that the magnitude of the corrosion attack was more profound and energetic at 600 s, since hydrogen development was only enhanced at 900 and 1200 s. The consumption rate decreased as the exposure period increased to 1500 s, indicating that the underlying eroding item obstructed the section of the consumption medium and secured metal substrates. Because a larger degree of pits, fractures, and fragments were created over the region, a greater corrosion rate occurs in 1500 s due to long chloride attack. Figure 24a–t depicts the corroded samples after different exposure times.

Figure 24a depicts the corroded morphology of A0 after 1200 s of exposure. It can be found that the alloy underwent severe pitting corrosion due to the absence of reinforcement. Because of the strong chloride attack, the pure aluminium layer breaks faster, resulting in more extensive formation of cracks and pits all over the surface of A0 as shown in SEM image Fig. 24f. The OM images in Fig. 25b–e show that Al_2O_3 reinforced nanocomposites were more corrosion resistant than A0. When the ions come into contact with the surface of the NaCl medium, they dissolve and generate copper-colored pits at different exposures [57]. The SEM image of nanocomposites are shown in Fig. 25g–j. The formation of micro-cracks, fragments, and pits on the corroded surface was observed in the SEM images. The surface of specimen A3 was found to be extensively corroded in the initial stages owing to the removal of an oxide coating on the surface. This was attributed to an increase in corrosion, which resulted in the formation of pits and cracks as seen in SEM images Fig. 25e–f. The OM Fig. 26c indicates that at 1200 s, the hydrogen ions produced hydroxide layer over the surface, which prevented pitting corrosion, as seen in

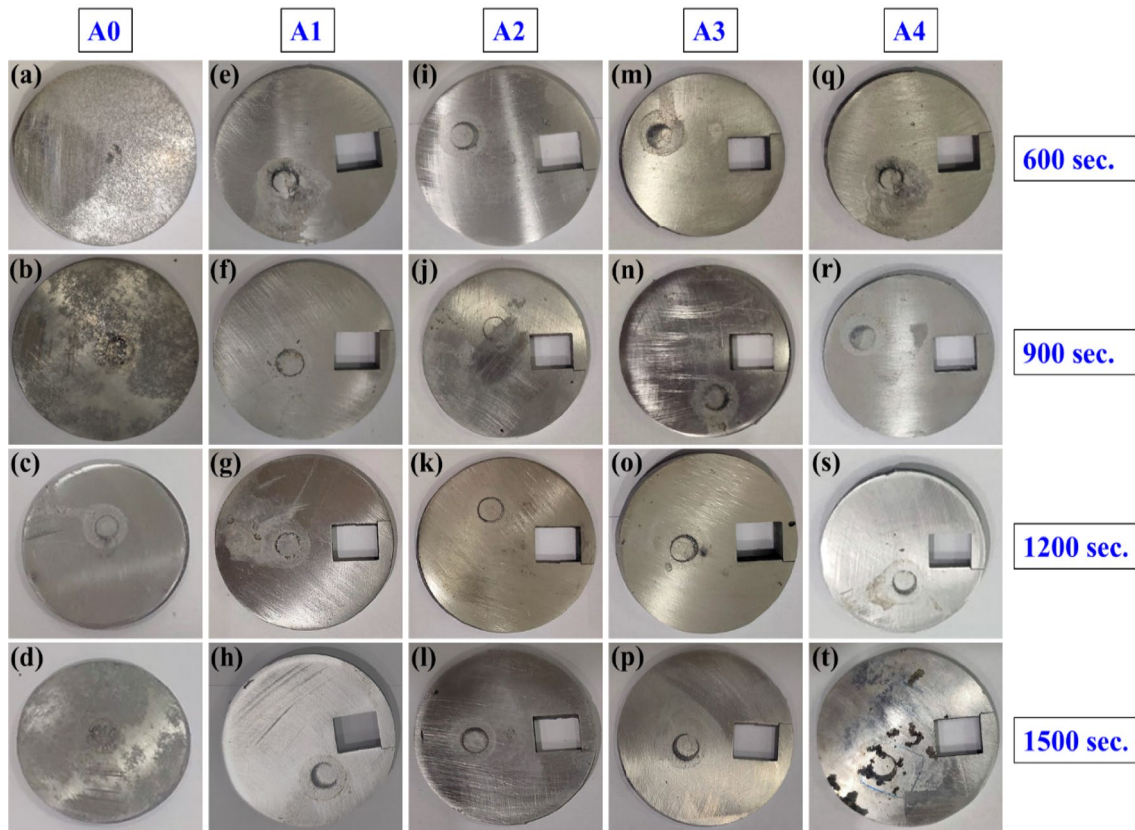


Fig. 24 a–t Electrochemically corroded samples at various exposure times

SEM image Fig. 26g [58]. Meanwhile, at higher exposures, Cl^- ions would destroy the $\text{Al}(\text{OH})_3$ layers. This surface disintegration caused aluminium composites to exhibit a variety of electrochemical responses. After the passive layer was broken, it encouraged severe corrosion at 1500 s through the formation of grooves and the micro-cracks as shown in Fig. 26e and j [59].

4 Conclusions

In this study, the AA2014/ Al_2O_3 nanocomposites were fabricated through the ultrasonic-assisted squeeze cast process by varying the reinforcement (1–4 wt%). The corrosion behaviour of specimens was analysed using tribocorrosion and electrochemical corrosion test methods with different exposure times 600, 900, 1200, and 1500 s. The following conclusions are drawn from this study.

- (1) The HR-SEM images of nanocomposites showed the homogeneous distribution of nanoparticles (up to 3 wt%) by ultrasonication in the AA2014 matrix. The XRD results of nanocomposites indicated the diffraction peaks of $\alpha\text{-Al}$, $\beta\text{-CuAl}_2$ and Al_2O_3 .
- (2) The addition of reinforcement increased the hardness and porosity of nanocomposites when compared to as-cast alloy. Maximum hardness was obtained for the nanocomposite A2 due to the uniform distribution of nanoparticles. A higher degree of porosity was observed in nanocomposite A4 due to the agglomeration of nanoparticles.
- (3) In the tribocorrosion test, the A3 exhibited a low OCP of -0.62 to -0.68 with a lower coefficient of friction 0.15 and a minimum current density of 4.889×10^{-4} at 900 s.
- (4) The passive film of alloy damaged by mechanical wear accelerated the material degradation with increasing the potential. However, due to the formation of alumina hydroxide protective layer, the corrosion rate in nanocomposites was minimized.

Fig. 25 Microstructure of electrochemically corroded samples at 1200 s **a–e** OM image and **f–j** SEM image

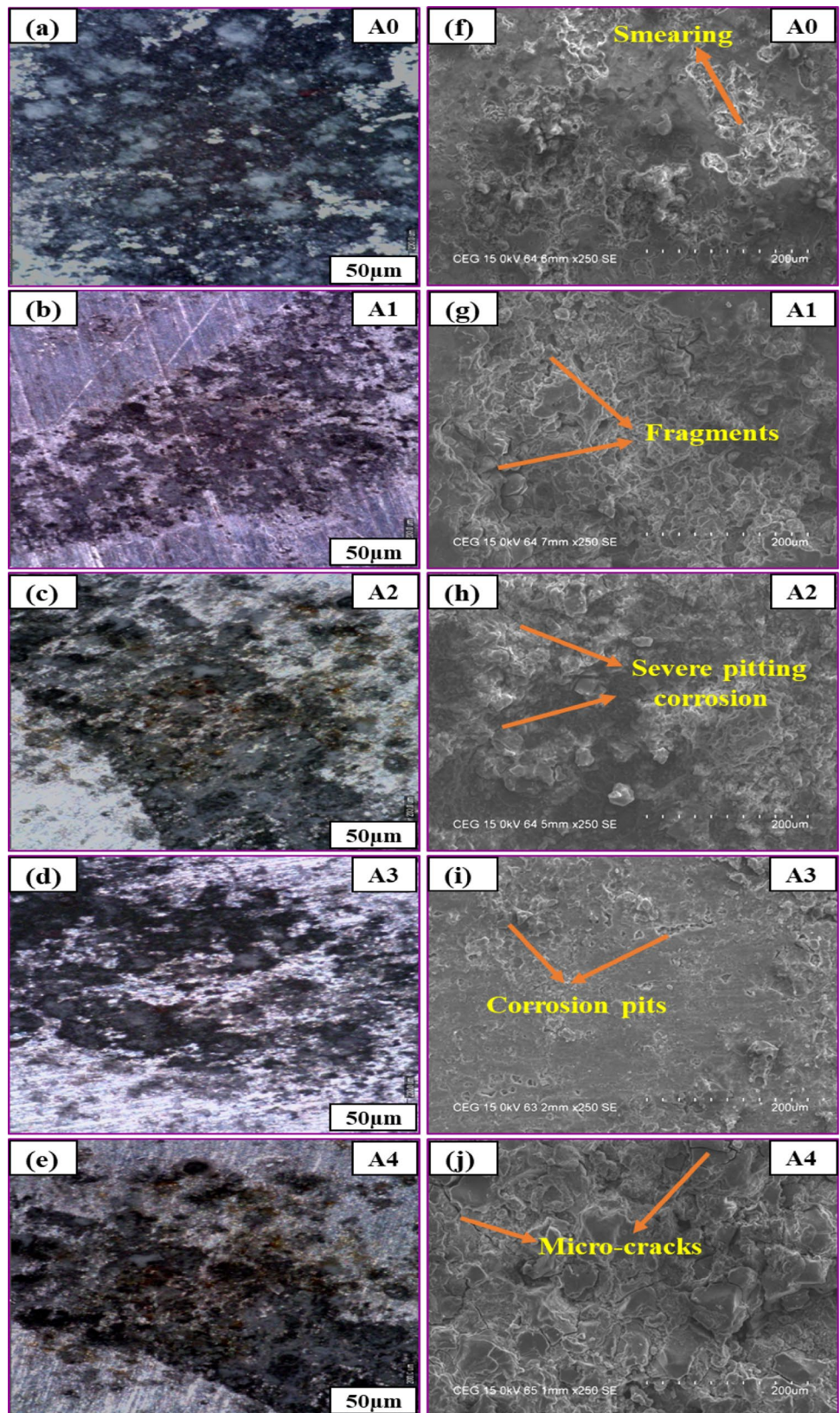
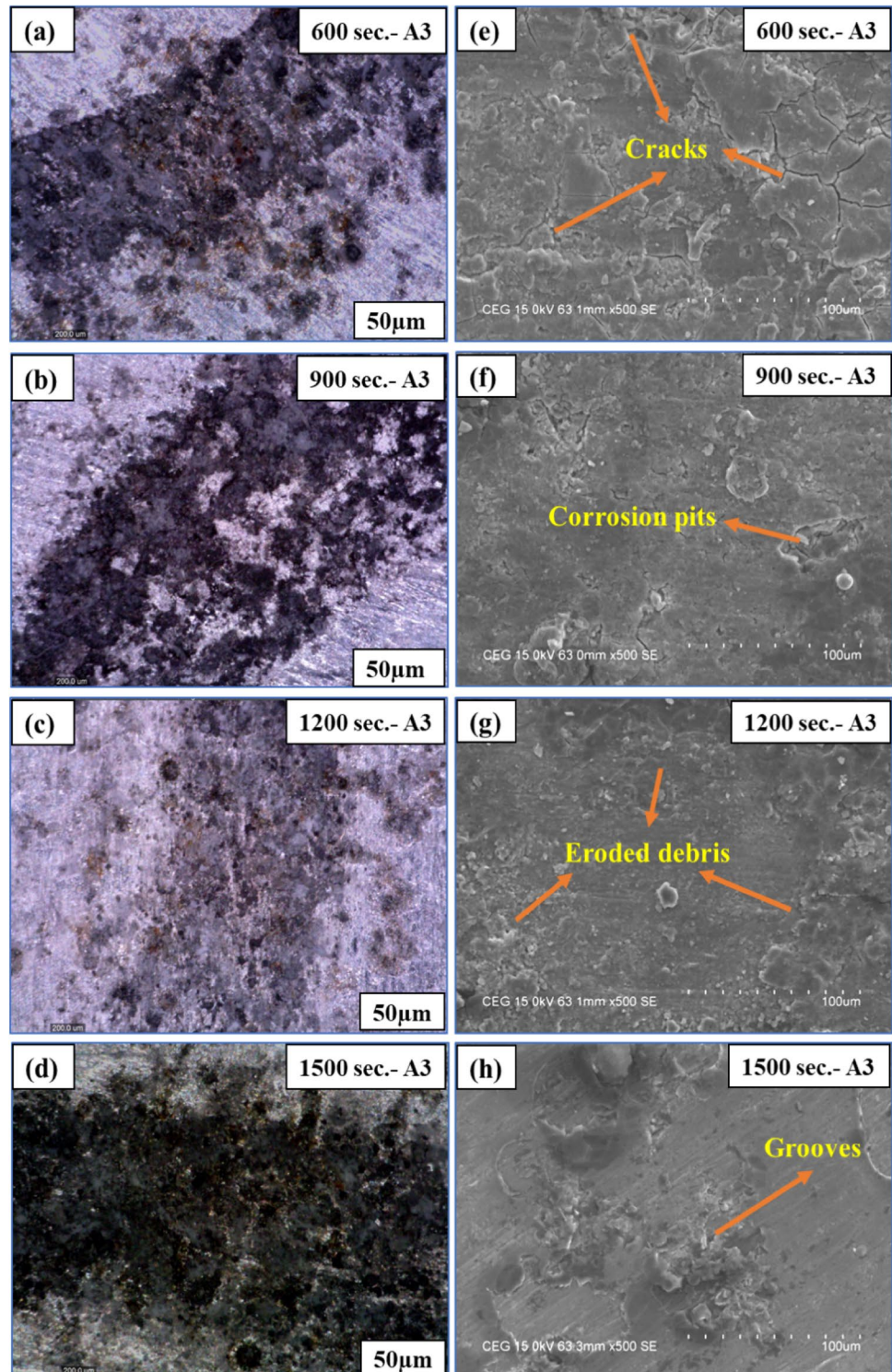


Fig. 26 a–d OM images and e–f SEM images of electrochemical sample A3 at different exposure times



(5) In the electrochemical corrosion test, the formation of a protective passive layer on composites A3 restricted the movement of ions compared to alloy and other nanocomposites. The addition of alumina nanoparticles helped in increasing the polarization resistance and restricted the plastic deformation in nanocomposites.

(6) At 1200 s, the composite A3 showed a minimal current density of 1.521×10^{-5} with an OCP value ranging from -0.4 to -0.5 V. The reaction occurred in the passive layer and ion dissolution phenomena were unavoidable corrosion factors when exposed to 3.5 wt% NaCl solution.

Acknowledgements The authors express their genuine gratitude to the Science and Engineering Research Board (SERB), Govt. of India, for funding this research work through the Grant Number: EEQ/2017/000382.

Data availability The raw/processed data required to reproduce these findings cannot be shared at this time as the data also forms part of an ongoing study.

Declarations

Conflict of interest The authors proclaim that they have no financial supremacy or personal relationship that could have influenced the work reported in this paper.

References

- Zhao Q, Guo C, Niu K et al (2021) Long-term corrosion behavior of the 7A85 aluminum alloy in an industrial-marine atmospheric environment. *J Mater Res Technol* 12:1350–1359. <https://doi.org/10.1016/j.jmrt.2021.03.085>
- Kannan C, Ramanujam R (2017) Comparative study on the mechanical and microstructural characterisation of AA 7075 nano and hybrid nanocomposites produced by stir and squeeze casting. *J Adv Res* 8:309–319. <https://doi.org/10.1016/j.jare.2017.02.005>
- André NM, Bouali A, Maawad E et al (2019) Corrosion behavior of metal–composite hybrid joints: influence of precipitation state and bonding zones. *Corros Sci* 158:108075. <https://doi.org/10.1016/j.corsci.2019.07.002>
- Usman BJ, Scenini F, Curioni M (2020) The effect of exposure conditions on performance evaluation of post-treated anodic oxides on an aerospace aluminium alloy: comparison between salt spray and immersion testing. *Surf Coat Technol* 399:126157. <https://doi.org/10.1016/j.surfcoat.2020.126157>
- Ramkumar KR, Sivasankaran S, Al-Mufadi FA et al (2019) Investigations on microstructure, mechanical, and tribological behaviour of AA 7075–x wt % TiC composites for aerospace applications. *Arch Civ Mech Eng* 19:428–438. <https://doi.org/10.1016/j.acme.2018.12.003>
- Khandelwal A, Mani K, Srivastava N et al (2017) Mechanical behavior of AZ31/Al₂O₃ magnesium alloy nanocomposites prepared using ultrasound assisted stir casting. *Compos Part B Eng* 123:64–73. <https://doi.org/10.1016/j.compositesb.2017.05.007>
- Dezfuli SM, Sabzi M (2018) Effect of yttria and benzotriazole doping on wear/corrosion responses of alumina-based nanostructured films. *Ceram Int* 44:20245–20258. <https://doi.org/10.1016/j.ceramint.2018.07.313>
- Raja S, Muhamad MR, Jamaludin MF, Yusof F (2020) A review on nanomaterials reinforcement in friction stir welding. *J Mater Res Technol* 9:16459–16487. <https://doi.org/10.1016/j.jmrt.2020.11.072>
- Maj J, Basista M, Węglewski W et al (2018) Effect of microstructure on mechanical properties and residual stresses in interpenetrating aluminum–alumina composites fabricated by squeeze casting. *Mater Sci Eng A* 715:154–162. <https://doi.org/10.1016/j.msea.2017.12.091>
- Bin SB, Xing SM, Tian LM et al (2013) Influence of technical parameters on strength and ductility of AlSi₉Cu₃ alloys in squeeze casting. *Trans Nonferrous Met Soc China (English Ed)* 23:977–982. [https://doi.org/10.1016/S1003-6326\(13\)62555-8](https://doi.org/10.1016/S1003-6326(13)62555-8)
- Loganathan P, Gnanavelbabu A, Rajkumar K (2021) Influence of ZrB₂/hBN particles on the wear behaviour of AA7075 composites fabricated through stir followed by squeeze cast technique. *Proc Inst Mech Eng Part J J Eng Tribol* 235:149–160. <https://doi.org/10.1177/1350650120929501>
- Jahangiri A, Marashi SPH, Mohammadaliha M, Ashofte V (2017) The effect of pressure and pouring temperature on the porosity, microstructure, hardness and yield stress of AA2024 aluminum alloy during the squeeze casting process. *J Mater Process Technol* 245:1–6. <https://doi.org/10.1016/j.jmatprotec.2017.02.005>
- Lu T, Chen W, Li B et al (2019) Influence mechanisms of Zr and Fe particle additions on the microstructure and mechanical behavior of squeeze-cast 7075Al hybrid composites. *J Alloys Compd* 798:587–596. <https://doi.org/10.1016/j.jallcom.2019.05.301>
- Gnanavelbabu A, Rajkumar K (2020) Experimental characterization of dimensional and surface alternation of straight and angular cutting on self-lubricating composite: a wire EDM approach. *Arab J Sci Eng* 45:5859–5872. <https://doi.org/10.1007/s13369-020-04596-2>
- Yuan D, Yang X, Wu S et al (2019) Development of high strength and toughness nano-SiCp/A356 composites with ultrasonic vibration and squeeze casting. *J Mater Process Technol* 269:1–9. <https://doi.org/10.1016/j.jmatprotec.2019.01.021>
- Idrisi AH, Mourad AHI (2019) Conventional stir casting versus ultrasonic assisted stir casting process: mechanical and physical characteristics of AMCs. *J Alloys Compd* 805:502–508. <https://doi.org/10.1016/j.jallcom.2019.07.076>
- Xu Z, Ma L, Yan J et al (2014) Solidification microstructure of SiC particulate reinforced ZneAl composites under ultrasonic exposure. *Mater Chem Phys* 148:824–832. <https://doi.org/10.1016/j.matchemphys.2014.08.057>
- Ayyanar S, Gnanavelbabu A, Rajkumar K, Loganathan P (2020) Studies on high temperature wear and friction behaviour of AA6061/B4C/hBN hybrid composites. *Met Mater Int*. <https://doi.org/10.1007/s12540-020-00710-z>
- Zhao J, Su H, Wu C (2020) The effect of ultrasonic vibration on stress-strain relations during compression tests of aluminum alloys. *J Mater Res Technol* 9:14895–14906. <https://doi.org/10.1016/j.jmrt.2020.10.094>
- Gnanavelbabu A, Sunu Surendran KT, Kumar S (2019) Influence of ultrasonication power on grain refinement, mechanical properties and wear behaviour of AZ91D/nano-Al₂O₃ composites. *Mater Res Express* 7:016544. <https://doi.org/10.1088/2053-1591/ab64d7>
- Deng X, Huang Z, Wang W, Davé RN (2016) Investigation of nanoparticle agglomerates properties using Monte Carlo simulations. *Adv Powder Technol* 27:1971–1979. <https://doi.org/10.1016/j.apt.2016.06.029>
- Gnanavelbabu A, Surendran KTS, Loganathan P, Vinothkumar E (2021) Effect of ageing temperature on the corrosion behaviour of UHTC particulates reinforced magnesium composites fabricated through ultrasonic assisted squeeze casting process. *J Alloys Compd* 856:158173856. <https://doi.org/10.1016/j.jallcom.2020.158173>
- Sharma S, Nanda T, Pandey OP (2019) Investigation of T4 and T6 heat treatment on the wear properties of sillimanite reinforced LM30 aluminium alloy composites. *Wear* 426–427:27–36. <https://doi.org/10.1016/j.wear.2018.12.065>
- Ananda Murthy HC, Bheema Raju V, Shivakumara C (2013) Effect of TiN particulate reinforcement on corrosive behaviour of aluminium 6061 composites in chloride medium. *Bull Mater Sci* 36:1057–1066. <https://doi.org/10.1007/s12034-013-0560-2>
- Fang Y, Chen N, Du G et al (2019) Effect of Y₂O₃-stabilized ZrO₂ whiskers on the microstructure, mechanical and wear resistance properties of Al₂O₃ based ceramic composites. *Ceram Int* 45:16504–16511. <https://doi.org/10.1016/j.ceramint.2019.05.184>
- Sundar A, Qi L (2021) Stability of native point defects in α -Al₂O₃ under aqueous electrochemical conditions. *J Appl Electrochem* 51:639–651. <https://doi.org/10.1007/s10800-020-01526-w>

27. Jun C, Bingli P, Quanan L (2020) Tribocorrosion behavior of LY12 aluminum alloy in artificial seawater solution tribocorrosion behavior of LY12 aluminum alloy in artificial seawater solution. *Tribol Trans* 63:1085–1094. <https://doi.org/10.1080/10402004.2020.1794091>
28. Cheng J, Ge Y, Wang B et al (2020) Microstructure and tribocorrosion behavior of Al₂O₃ / Al composite coatings: role of Al₂O₃ addition. *J Therm Spray Technol* 29:1741–1751. <https://doi.org/10.1007/s11666-020-01062-1>
29. Huttunen-Saarivirta E, Isotahdon E, Metsäjoki J et al (2018) Tribocorrosion behaviour of aluminium bronze in 3.5 wt % NaCl solution. *Corros Sci* 144:207–223. <https://doi.org/10.1016/j.corsci.2018.08.058>
30. Abolusoro OP, Akinlabi ET (2020) Tribocorrosion measurements and behaviour in aluminium alloys: an overview. *J Bio-Tribo-Corros* 6:102. <https://doi.org/10.1007/s40735-020-00393-4>
31. Sinhmar S, Dwivedi DK (2018) A study on corrosion behavior of friction stir welded and tungsten inert gas welded AA2014 aluminium alloy. *Corros Sci* 133:25–35. <https://doi.org/10.1016/j.corsci.2018.01.012>
32. Gharavi F, Matori KA, Yunus R et al (2016) Corrosion evaluation of friction stir welded lap joints of AA6061-T6 aluminum alloy. *Trans Nonferrous Met Soc China* 26:684–696. [https://doi.org/10.1016/S1003-6326\(16\)64159-6](https://doi.org/10.1016/S1003-6326(16)64159-6)
33. Roseline S, Paramasivam V (2019) Corrosion behaviour of heat treated aluminium metal matrix composites reinforced with fused zirconia alumina 40. *J Alloys Compd* 799:205–215. <https://doi.org/10.1016/j.jallcom.2019.05.185>
34. Sundaram PA (2016) Corrosion behavior of novel Al-Al₂O₃ composites in aerated 3.5% chloride solution. *J Mater Eng Perform* 26:69–75. <https://doi.org/10.1007/s11665-016-2420-x>
35. Ugender S, Kumar A, Reddy AS (2014) Experimental Investigation of tool geometry on mechanical properties of friction stir welding of AA 2014 aluminium alloy. *Procedia Mater Sci* 5:824–831. <https://doi.org/10.1016/j.mspro.2014.07.334>
36. Zhang Y, Yi Y, Huang S, He H (2017) Influence of temperature-dependent properties of aluminum alloy on evolution of plastic strain and residual stress during quenching process. *Metals (Basel)* 7:228. <https://doi.org/10.3390/met7060228>
37. Xu J, Chen G, Zhang Z et al (2021) Effect of Al-3wt %Al₂O₃ master alloy fabricated by calcined kaolin on grain refinement and mechanical properties of A356 alloy. *J Alloys Compd* 862:158512. <https://doi.org/10.1016/j.jallcom.2020.158512>
38. Ji Y, Fu R, Lv J et al (2020) Enhanced bonding strength of Al₂O₃ / AlN ceramics joined via glass frit with gradient thermal expansion coefficient. *Ceram Int* 46:12806–12811. <https://doi.org/10.1016/j.ceramint.2020.02.050>
39. Hima Gireesh C, Durga Prasad K, Ramji K (2018) Experimental investigation on mechanical properties of an al6061 hybrid metal matrix composite. *J Compos Sci* 2:49. <https://doi.org/10.3390/jcs2030049>
40. Ma P, Jia Y, Gokuldoss PK et al (2017) Effect of Al₂O₃ nanoparticles as reinforcement on the tensile behavior of Al-12Si composites. *Metals (Basel)* 7:1–11. <https://doi.org/10.3390/met7090359>
41. Reddy C (2011) Evaluation of mechanical behavior of Al-Alloy / Al₂O₃ metal matrix composites with respect to their constituents using taguchi technique. *I-manager's J Mech Eng* 4:26–32. <https://doi.org/10.26634/jme.1.2.1405>
42. Liew KM, Kai MF, Zhang LW (2016) Carbon nanotube reinforced cementitious composites: an overview. *Compos Part A Appl Sci Manuf* 91:301–323. <https://doi.org/10.1016/j.composita.2016.10.020>
43. Silva JI, Alves AC, Pinto AM, Toptan F (2017) Corrosion and tribocorrosion behavior of Ti–TiB–TiNx in-situ hybrid composite synthesized by reactive hot pressing. *J Mech Behav Biomed Mater* 74:195–203. <https://doi.org/10.1016/j.jmbbm.2017.05.041>
44. Heidarpour A, Mousavi ZS, Karimi S, Hosseini SM (2021) On the corrosion behavior and microstructural characterization of Al2024 and Al2024/Ti2SC MAX phase surface composite through friction stir processings. *J Appl Electrochem*. <https://doi.org/10.1007/s10800-021-01567-9>
45. Shrivastava V, Singh P, Kumar G (2021) Synergistic effect of heat treatment and reinforcement content on the microstructure and corrosion behavior of Al-7075 alloy based nanocomposites. *J Alloys Compd* 857:157590. <https://doi.org/10.1016/j.jallcom.2020.157590>
46. Umoren SA, Li Y, Wang FH (2011) Effect of aluminium microstructure on corrosion and inhibiting effect of polyacrylic acid in H₂SO₄ solution. *J Appl Electrochem* 41:307–315. <https://doi.org/10.1007/s10800-010-0240-5>
47. Bonfils-Lahovary ML, Laffont L, Blanc C (2017) Characterization of intergranular corrosion defects in a 2024 T351 aluminium alloy. *Corros Sci* 119:60–67. <https://doi.org/10.1016/j.corsci.2017.02.020>
48. Safiuddin M (2017) Concrete damage in field conditions and protective sealer and coating systems. *Coatings* 7:90. <https://doi.org/10.3390/coatings7070090>
49. Abdel-Gawad SA, Osman WM, Fekry AM (2019) Characterization and corrosion behavior of anodized aluminum alloys for military industries applications in artificial seawater. *Surf Interfaces* 14:314–323. <https://doi.org/10.1016/j.surfint.2018.08.001>
50. Machkova MS, Kozhukharov VS (2014) Influence of buffering on the spontaneous deposition of cerium conversion coatings for corrosion protection of AA2024-T3 aluminum alloy. *J Appl Electrochem* 44:1093–1105. <https://doi.org/10.1007/s10800-014-0718-7>
51. Rodrı P (2014) The electrochemical characteristics of commercial aluminium alloy electrodes for Al / air batteries. *J Appl Electrochem* 44:1371–1380. <https://doi.org/10.1007/s10800-014-0751-6>
52. Luo C, Albu SP, Zhou X et al (2016) Continuous and discontinuous localized corrosion of a 2xxx aluminium-copper-lithium alloy in sodium chloride solution. *J Alloys Compd* 658:61–70. <https://doi.org/10.1016/j.jallcom.2015.10.185>
53. Jayaraj RK, Malarvizhi S, Balasubramanian V (2017) Electrochemical corrosion behaviour of stir zone of friction stir welded dissimilar joints of AA6061 aluminium–AZ31B magnesium alloys. *Trans Nonferrous Met Soc China (English Ed)* 27:2181–2192. [https://doi.org/10.1016/S1003-6326\(17\)60244-9](https://doi.org/10.1016/S1003-6326(17)60244-9)
54. Liu S, Wang B (2020) Electrochemical corrosion behavior of a magnesium calcium alloy in simulated body fluids with different glucose concentrations. *J Mater Res Technol* 9:6612–6619. <https://doi.org/10.1016/j.jmrt.2020.04.052>
55. Zhang Z, Liu F, Han E et al (2019) Effects of Al₂O₃ on the microstructures and corrosion behavior of low- pressure cold gas sprayed Al 2024-Al₂O₃ composite coatings on AA 2024–T3 substrate. *Surf Coat Technol* 370:53–68. <https://doi.org/10.1016/j.surfcoat.2019.04.082>
56. Thirumalaikumarasamy D, Shanmugam K, Balasubramanian V (2014) Comparison of the corrosion behaviour of AZ31B magnesium alloy under immersion test and potentiodynamic polarization test in NaCl solution. *J Magnes Alloys* 2:36–49. <https://doi.org/10.1016/j.jma.2014.01.004>
57. Arthanari S, Nallaiyan R, Kwang Seon S (2017) Electrochemical corrosion behavior of acid treated strip cast AM50 and AZX310 magnesium alloys in 3.5 wt% NaCl solution. *J Magnes Alloys* 5:277–285. <https://doi.org/10.1016/j.jma.2017.08.001>
58. Faegh E, Shrestha S, Zhao X, Mustain WE (2019) In—depth structural understanding of zinc oxide addition to alkaline

- electrolytes to protect aluminum against corrosion and gas-
sing. *J Appl Electrochem* 49:895–907. <https://doi.org/10.1007/s10800-019-01330-1>
59. Smoljko I, Gudic S, Kuzmanic N et al (2012) Electrochemical properties of aluminium anodes for Al/air batteries with aqueous sodium chloride electrolyte. *J Appl Electrochem* 42:969–977. <https://doi.org/10.1007/s10800-012-0465-6>

Publisher's Note Springer Nature remains neutral with regard to jurisdictional claims in published maps and institutional affiliations.